Early underdetected dissemination followed by extensive local transmission propelled the 2022 mpox epidemic and limited impact of vaccination

Miguel I. Paredes[1,2*], Nashwa Ahmed[2,3], Marlin Figgins[2,4], Vittoria Colizza[5], Philippe Lemey[6], John T. McCrone[2], Nicola Müller[2], Cécile Tran-Kiem[2], Trevor Bedford[1,2,7]

Affiliations

[1] Department of Epidemiology, University of Washington, Seattle, Washington, USA
[2] Vaccine and Infectious Disease Division, Fred Hutchinson Cancer Center, Seattle, Washington, USA
[3] Molecular and Cellular Biology Program, University of Washington, Seattle, WA, USA
[4] Department of Applied Mathematics, University of Washington, Seattle, WA, USA
[5] INSERM, Sorbonne Université, Institut Pierre Louis d'Epidémiologie et de Santé Publique IPLESP, Paris, France
[6] Department of Microbiology, Immunology and Transplantation, Rega Institute, KU Leuven, Leuven, Belgium
[7] Howard Hughes Medical Institute, Seattle, WA, USA
[*]*Corresponding author. Email: paredesm@uw.edu*

Abstract: (word count: 200, currently 200)
The World Health Organization (WHO) declared mpox a public health emergency of international concern in July 2022. It is still unclear to what extent international travel contributed to the explosive spread of mpox and the degree to which national vaccination campaigns were responsible for controlling the epidemic. We built phylogeographic and phylodynamic models to analyze MPXV genomes sampled between March 2022 and January 2023 from five global regions together with air traffic and epidemiological data to analyze the global spread of mpox. Our models reveal community transmission prior to detection by local surveillance, changes in case-reporting throughout the epidemic, and a large degree of transmission heterogeneity. Additionally, we find that viral introductions played a limited role in prolonging spread after initial dissemination, suggesting that travel bans would have had only a minor impact. We find that the time-varying effective reproductive number in North America declines below one before more than 10% of individuals at high risk individuals in the USA had vaccine-induced immunity, suggesting little impact of vaccination in controlling the epidemic. Given that cases quickly declined after detection most likely due to behavioral modifications, our findings highlight the importance of broader routine specimen screening surveillance for emerging infectious diseases.

Introduction

Mpox is a viral zoonotic disease caused by the mpox virus (MPXV), previously referred to as monkeypox virus, that is endemic to West and Central Africa (1,2). Prior to 2022, most cases of mpox outside of endemic regions occurred in individuals with either a recent travel history to Nigeria or with an exposure to live animals from endemic areas. On May 7, 2022, an individual with a travel history to Nigeria was diagnosed with mpox in the United Kingdom (UK) (3). Following this initial detection, the number of mpox cases without a travel history to endemic countries began to increase rapidly in various regions around the globe consistent with epidemic human-to-human spread (3). As of July 19, 2023, the Centers for Disease Control and Prevention (CDC) reported 88,549 cases of mpox worldwide since Jan 2022 (4).

The 2022 mpox epidemic was characterized by human-to-human spread outside of endemic areas, mostly in men who have sex with men (MSM), that resulted in a less severe illness presentation compared to what was seen in historical short human-to-human transmission chains following repeated zoonoses (2,3,5). The long incubation period of 5-21 days (3,6), as well as the atypical and less severe illness presentation suggests that mpox may have spread undetected prior to initial case discovery. Presymptomatic transmission of mpox has also been documented, suggesting that the epidemic was at least partially fueled by transmission occurring prior to symptom onset (7–9).

The WHO declared mpox to be a public health emergency of international concern on July 23, 2022, promoting investigations into disease spread, the use of vaccines to control transmission, and potential guidelines for international travel (10). Individual countries began vaccination efforts in an attempt to curb mpox spread but have been criticized for long delays in starting effective vaccination campaigns in high-risk areas (11). To date, it is still unclear to what extent continued international travel contributed to the explosive spread of mpox in various global regions and whether or not national vaccination campaigns were responsible for controlling the epidemic.

Genomic epidemiology is uniquely poised to explore global and regional transmission dynamics through the joint integration of viral genomic information and epidemiological metadata. This approach augments traditional public health surveillance, especially when case-based surveillance is limited (12). While a few studies have looked into the regional spread of mpox at various stages of the 2022 epidemic (13–16), most relied on very few pathogen genomes. Overall, the extent of undetected mpox spread and the effectiveness of proposed interventions have yet to be examined. Here we employ recent advances in phylogeographic and phylodynamic methods to estimate changes in case detection rate and the role of introductions in promoting local community spread in various global regions. We also examine the impact of

vaccination on epidemic growth and decay in North America as well as estimate the degree of transmission heterogeneity in the declining phase of the epidemic.

Methods

Genomic data and maximum likelihood tree generation

All available MPXV sequences were downloaded from GenBank while excluding sequences from countries with five or fewer sequences, leaving Austria, Belgium, Canada, Colombia, France, Germany, Italy, Peru, Portugal, Slovakia, Slovenia, Spain, Switzerland, United Kingdom, and the USA. Sequences with ambiguous dates in the month column, with a sample collection earlier than January 2022, and flagged as being low quality by Nextclade (17) were excluded. Given that the 2022 epidemic was found to be driven by MPXV clade II, lineage B (14,18), any sequences not part of lineage B were also excluded, resulting in 3013 genome sequences included in our analysis.

A temporally-resolved phylogeny was created using a modified version of the Nextstrain (19) monkeypox workflow (https://github.com/nextstrain/monkeypox), which aligns sequences against the MPXV_USA_2021_MD (accession ON918611) reference using nextalign (17), infers a maximum-likelihood phylogeny using IQ-TREE (20) with a GTR nucleotide substitution model, and estimates molecular clock branch lengths using TreeTime (21). The resulting phylogeny specific to this dataset can be found at https://nextstrain.org/groups/blab/monkeypox/hmpxv1.

Regional geographic scales

Due to the low number of sequences from various countries, we analyzed mpox spread at the scale of global regions. We focused on five regions with the highest number of publicly available sequences on Genbank: Central Europe, North America, South America, Southern Europe, and Western Europe. Country to region mapping can be found in Supplementary Table 1.

Data Sources

Data on the number of reported mpox cases per region per month were downloaded from OWID (https://ourworldindata.org/; last accessed on February 13 2023).

Population sizes for each country were downloaded from the World Bank (https://data.worldbank.org/indicator/SP.POP.TOTL) and aggregated based on respective countries and then regions as described in the previous section.

To compare vaccination rates with changes in *Rt*, we accessed publicly available vaccination counts from the CDC (https://www.cdc.gov/poxvirus/mpox/response/2022/vaccines_data.html) as well as the cumulative percentage of high risk individuals vaccinated (22). In order to account

for the development of immunity, we followed the CDC method of assuming the development of immunity took two weeks following vaccination (22).

We used air travel data from the International Air Transport Association (IATA) quantifying the monthly number of passengers on origin-destination itineraries between airports in the 15 included countries (23).

Site masking

We found that fewer than 0.01% of nucleotide positions out of 197,209 total sites in the MPXV sequence alignment were phylogenetically informative, ie. polymorphic. To reduce computational runtime for phylogeographic reconstruction (discrete trait analysis), we masked 90% of invariant positions from the MPXV alignment prior to further analysis. The Nextstrain monkeypox workflow produces a BED file containing phylogenetically uninformative or misleading alignment positions to be masked. A VCF file was generated from the alignment using SNP-sites v2.5.1 (24). We identified variable positions from the VCF using Pysam v0.20.0 (25). Next, we selected a random subset of 90% of all invariant positions to remove and appended the remaining nucleotides to the BED file. A new alignment of 19,721 positions was generated with the modified BED file using the Nextstrain workflow.

Phylogeographic analysis

To investigate the dispersal history of MPXV among five global regions, we first conducted an asymmetric discrete trait phylogeographic analysis (26) using the Bayesian stochastic search variable selection (BSSVS) model implemented in BEAST 1.10 (27). For this analysis, we considered each global region as a discrete location and employed subsampling weighted by mpox case counts for each region, resulting in a final subset of 1004 sequences (distribution across countries and regions shown in Supplementary Table 1). We masked the alignment as described above. We employed a strict molecular clock with a uniform distribution from 0 to 1 and an initial value of 6×10^{-5} and a GTR+Γ nucleotide substitution model. We used a Skygrid coalescent tree prior allowing grid points to change every two weeks (28). Two independent Markov chain Monte Carlo (MCMC) procedures were run for 5×10^{8} iterations and sampled every 1000 iterations. Resulting posterior distributions were combined after discarding initial 20% of sampled trees as burn-in from each of them. We used Tracer 1.7 (29) to assess convergence and to estimate effective sampling size (ESS). These values were all >150. We then used TreeAnnotator 1.10 to obtain a maximum clade credibility (MCC) tree removing the first 20% of iterations for burn-in.

The number of viral imports and exports between regions was estimated by calculating the number of regional transitions walking from tips to root in the posterior set of trees and calculating the median as well as the 50% and 95% highest posterior density estimates (HPD). Following Bedford et al. (30), persistence time was measured by calculating the average number

of days for a lineage to leave its sampled region, walking backwards up the phylogeny from the tip up until the node location was different from the tip region.

In a secondary analysis, in order to check the accuracy of ancestral state reconstructions as well as the strength of genomic signal, out of the same 1004 sequences, 10% had their locations masked and then reconstructed (31) via the same discrete trait analysis described above. Reconstruction accuracy was assessed by comparing the most likely reconstructed location with the true location.

Estimation of mpox incidence, prevalence, and effective reproduction number via case counts
To jointly estimate mpox case incidence, prevalence, and effective reproduction number, we used the renewal equation framework from Figgins and Bedford (32) assuming a single variant. The time-varying effective reproduction number (i.e. the average number of secondary cases infected by a single primary case) was modeled using a 4th order spline with 5 evenly spaced knots assuming a discretized gamma-distributed generation time with mean 12.6 days and standard deviation 5.7 days (6). Case counts were modeled using a zero-inflated negative binomial distribution. This model produces posterior estimates of daily incidence (defined as the number of newly infected individuals in absolute counts) and effective reproduction number. We then used this incidence and an assumed gamma-distributed infectious period with a mean of 4.5 days to compute the prevalence, which we define as the number of actively infected individuals in absolute counts (6).

Models were fit to aggregated case counts for each region using full-rank stochastic variational inference. Optimization was performed using the ADAM optimizer with learning rate 4e-3 and for 50,000 iterations and 500 samples were drawn from the approximate posterior.

Estimated importation intensity
We estimated the monthly importation intensity of mpox between the five selected global regions between May and December 2022 using air travel data, estimated regional prevalence and regional human population size. The monthly estimated importation intensity (EII) is an estimate of the number of mpox cases imported into each region during a given month, calculated as

$$EII_a(t) = \sum_{i\,!=a} \frac{P_i(t)}{T_i} \times n_{i\to a}(t),$$

where (EII for region *a* at month *t* is computed using the estimated mpox prevalence $P_i(t)$ in a different region i, the population size T_i in region i and the number $n_{i\to a}(t)$ of air passengers traveling from region *i* to region *a* (adapted from Fauver et al.(33)). The sum over every global region excluding domestic travel. We used the prevalence estimates obtained from case data as described in the previous paragraph.

MASCOT GLM

To analyze the transmission dynamics within and between each global region, we used an adapted version of MASCOT (34). MASCOT is an approximate structured coalescent approach (35) that models how lineages coalesce (share a common ancestor) within the same locations and migrate between locations. We used generalized log-linear models (36) to estimate whether estimated regional mpox prevalence and air passenger volumes are predictive of MPXV effective population sizes and migration rates over time, respectively. Additionally, in order to account for differential underreporting by month, ten additional effective population size predictors were added, one for every month of the time period studied from April 2022 through January 2023. Empirical predictors were obtained via data sources described above. The model included error terms to account for observation noise and omitted predictor variables. We implemented a MASCOT-GLM (36) analysis with BEAST2 (37) software, allowing the effective population sizes and the migration rates to change every week. We performed effective population size and migration rate inference using an adaptive multivariate Gaussian operator (38) and ran the analyses using an adaptive Metropolis-coupled MCMC (39) using four chains with a length of 2.5×10^8. For this analysis, we employed equal temporal subsampling to enrich for undersampled regions by randomly choosing a max of 11 sequences per region per calendar month via Augur filter (40), resulting in 587 included sequences. No alignment masking was conducted for MASCOT analyses.

MASCOT- Skyline

In order to investigate the degree of genomic signal and influence of empirical predictors on tree reconstruction, we reran our MASCOT analysis without empirical predictors using a MASCOT-Skyline approach. To allow for population sizes to change over time, we modeled the effective population sizes similar to the Skygrid approach for unstructured populations (28). We estimated the effective population size for each location between time t=0×tree height, …, t=1×tree height. Between each time point where we estimated the *Ne*, we assumed exponential growth. *A priori*, we assumed that the effective population size at time t+1 is normally distributed with mean 0 and standard deviation σ, with σ being estimated. We assumed the migration rate to be constant forward-in-time, m^{f}_{zy}, between states y and z . As the structured coalescent assumes backwards-in-time migration rates, we assumed that the backwards-in-time rate of migration between state y and z, m^{b}_{yz} is $= m^{f}_{zy} \times \frac{Ne(t)_z}{Ne(t)_y}$. To infer effective population sizes and migration rates over time, we employed an adaptable multivariate gaussian operator (38).

Posterior processing

Parameter traces were visually evaluated for convergence using Tracer, tree distributions were visually inspected using IcyTree (41), and 20% burn-in was applied for all phylodynamic

analyses. All tree plotting was performed with baltic (https://github.com/evogytis/baltic) and data plotting was done using Altair (42).

Estimating percentage of new cases due to introductions

We estimated the percentage of new cases due to introductions for each global region by adapting the methods previously described (43,44). The percentage of cases due to introductions π at time *t* can be calculated by dividing the number of introductions at time *t* by the total number of new cases at time *t*. We first represented the total number of new cases in a region as the sum of the number of introductions and the number of new local infections due to local transmission, resulting in the following equation:

$$\pi(t) = \frac{\#\ of\ introductions(t)}{\#\ of\ new\ local\ cases(t) + \#\ of\ introductions(t)}.$$

We estimated the number of new local cases at time *t* by assuming the local epidemic in each global region follows a simple transmission model, in which we derived the number of new cases at time *t* as the product of the transmission rate β (new infections per day per individual) multiplied by the number of people already infected in that region *I*. For the number of introductions, we similarly assumed that the number of introductions equals the product of the rate of introduction (introductions per day per infectious individual, which we refer to as migration rate *m*) and the number of people already infected in that region *I*. We use the number of infected individuals in the destination region rather than the origin region for calculating the number of introductions since the approximate structured coalescent approach models epidemic processes as backwards-in-time, resulting in the equation containing only information about the number of infected individuals in the destination region (more information on backwards migration rates below). We then rewrote the above equation as

$$\pi(t) = \frac{m(t)\, I(t)}{\beta(t)\, I(t) + m(t)\, I(t)},$$

where $I(t)$ denotes the number of infected people in that region at time *t*. Given the presence of $I(t)$ in every element, we factored out $I(t)$ to arrive at

$$\pi(t) = \frac{m(t)}{\beta(t) + m(t)}.$$

For each region, we considered introductions at time *t* to be the sum of the introductions coming into the region from each other global region, assuming a negligible number of introductions from unincluded regions. We define the percentage of new cases due to introductions π at time *t* for region *y* as

$$\pi_y(t) = \frac{\sum_{i != y} m_{i \to y}(t)}{\beta_y(t) + \sum_{i != y} m_{i \to y}(t)},$$

where $m_{i \to y}$ denotes the migration rate per lineage per day into region *y* from every other region.

In a SEIR transmission modeling framework (employed due to the incubation period of MPXV), the transmission rate β is a function of the infectious period γ, the incubation period σ, and the exponential growth rate *r (*as adapted from Ma 2020 (45)):

$$\beta = \frac{(2r+\delta+\sigma)^2 - (\sigma-\gamma)^2}{4\sigma}$$

To compute the growth rate in region *y*, we assumed that differences in effective population size between adjacent time intervals can approximate the growth rate *r* and thus $\frac{d(log(Ne_y)}{dt} \approx r$. In addition, we assumed that $\frac{dNe}{dt}$ is independent from the rate of introduction. We calculated the growth rate of the effective population size $\frac{dNe}{dt}$ as

$$\frac{d(log(Ne))}{dt} = \frac{log(Ne(t+\Delta t)) - log(Ne(t))}{\Delta t},$$

where $Ne(t)$ denotes the effective population size of a region at time *t*. We ran our MASCOT-GLM analysis using weekly time intervals but averaged over three week intervals (Δt = 3) for the growth rate in order to reduce noise and account for the long generation time for mpox.

By also assuming an expected time until becoming uninfectious for each individual of 4.5 days and an incubation period of 8 days (6), we calculated the transmission rate β at time *t* in region *y* as

$$\beta_y(t) = \frac{(2(\frac{dNe_y}{dt})+\delta+\sigma)^2 - (\sigma-\gamma)^2}{4\sigma}.$$

Since the coalescent, which MASCOT approximates, works backward-in-time, we calculated the rate of introductions into each global region $m_y(t)$ as the backwards migration rate $m^b{}_y(t)$ from inferred MASCOT parameters. To compute the backwards migration rate, we extract the forward-in-time migration rate $m^f{}_{yi}(t)$, where *i* refers to a different region in a combination of global regions *c,* that is inferred via MASCOT-GLM, and then calculate the backwards-in-time migration rate into region *y*, as the sum of the products of the ratio of effective population sizes $\frac{Ne_y(t)}{Ne_z(t)}$ and the forward migration rates:

$$m^{b}_{y}(t) = \sum_{i=1}^{c} \frac{Ne_{y}(t)}{Ne_{i}(t)} \times m^{f}_{yi}(t),$$

where $Ne_{y}(t)$ refers to the effective population size in region y at time *t* and $Ne_{i}(t)$ refers to the effective population size in a different region *i* from a combination of global regions *c* at time *t*.

Estimating the effective reproductive number Rt from pathogen genomes

We calculated the effective reproductive number *Rt*, the time-varying average of secondary infections from a primary infected individuals, in each region, assuming an exponentially distributed infectious and incubation period of mean respectively $1/\gamma$ and $1/\sigma$, yielding $Rt = (1 + \frac{r}{\gamma})(1 + \frac{r}{\sigma})$ (46). Additionally, we sought to separate out the contributions of introductions versus local transmission to Rt_t in each region. To do so, we modified the *Rt* equation to include the percent of new cases from introductions as an estimate of local community spread so that $Rt = (1 + \frac{r}{\gamma})(1 + \frac{r}{\sigma})(1 - \pi)$, where π refers to the percentage of new cases due to introductions as described above.

Estimating transmission heterogeneity

We analyzed the size distribution of clusters of identical mpox sequences to characterize the disease's offspring distribution (47). We assumed that the offspring distribution follows a negative binomial distribution characterized by its reproduction number *R* and its dispersion parameter *k* (48). The probability r_j that a cluster of identical sequences of size *j* can be derived as

$$r_j = \frac{\Gamma(kj+j-1)}{\Gamma(kj) \times \Gamma(j+1)} \times \frac{(\frac{pR}{k})^{j-1}}{(1+\frac{pR}{k})^{j-1}},$$

where p denotes the probability that a transmission event occurs before a mutation event.

In practice, only a fraction of infections are sequenced. The probability $\tilde{r}_j$ to observe a cluster of size *j* was thus derived as:

$$\tilde{r}_j = \frac{\sum_{l \geq j} r_l \binom{l}{j} (p_{detect})^{j} (1-p_{detect})^{l-j}}{1 - \sum_{l \geq 0} r_l (1-p_{detect})^{l}}$$

where p_{detect} denotes the fraction of infections sequenced.

The probability for an observed cluster of identical sequences to be of size at least J can then be computed as $P_J = 1 - \sum_{j=1}^{J-1} \tilde{r}_j$. The probability to observe at least a cluster of size J among n_{clust} clusters is thus equal to $1 - (1 - P_J)^{n_{clust}}$.

Former work has shown that the size distribution of clusters of identical sequences can be used to infer the reproduction number and the dispersion parameter when the mean number of offspring with identical sequences lies below 1 (47). For the 2022 mpox epidemic, this would correspond to values of the reproduction number lying below 1.5 (47). To ensure this criterion was met, we analyzed the size distribution of clusters of identical mpox sequences for different geographical units (Portugal, the United Kingdom and US states California, New York and Washington) from August 2022, which corresponds to the decreasing phase of the epidemic (Supp Fig. 8). We generated the size distribution of clusters of identical mpox sequences for these different geographical units and defined clusters temporally based on their date of first detection. We estimated the fraction of cases sequenced in these different regions from August 2022 by computing the ratio between the number of sequences used and the number of cases publicly reported. We first inferred the parameters of the offspring distribution assuming that the dispersion parameter was the same across these geographical units and estimating a reproduction number for each of these geographical units. This was done by considering different assumptions regarding the fraction of infections detected (10%, 50% and 100%) and assuming a probability that transmission occurs before mutation equal to 66% (46) .We also ran a location-specific model and estimated the reproduction number and the dispersion parameter for these each region. We assumed that clusters of identical sequences stemmed from local transmission dynamics. This hypothesis is supported by the small contribution played by introductions estimated from the phylogeographic analysis.

We also generated the distribution of cluster sizes worldwide. We explored how different assumptions regarding R and k impacted the probability to observe a cluster of size 118 (the largest cluster observed) among the 2624 clusters of identical sequences observed. This was done assuming that 5.5% of infections were sequenced (which corresponds to the fraction of cases sequenced since the beginning of the epidemic).

Data Availability

Nextstrain builds, BEAST XMLs, scripts, sequence information, and de-identified data can be found at https://github.com/blab/mpox-dynamics.

Results

Early mpox spread in Western Europe sparks prolonged outbreaks in Southern Europe, North America and South America

Following initial detection in the UK on May 7, 2022, the number of mpox cases reported worldwide grew rapidly (Fig. 1). In early May, reported cases were found mainly in Western and Southern, and then Central, Europe where the epidemic peaked around mid-July (Fig 1A, B). Beginning in mid-May, however, cases began to be reported in North America, which ultimately led to the largest number of reported cases of any global region studied, peaking at the beginning of August. Around the same time as the North American peak, cases were detected and started rising in South America, which substantially contributed to the later tail of the 2022 mpox epidemic. Similarly, the number of sequences collected increased as more cases were detected, with heterogeneity between regions and North America (primarily the US) submitting the largest number of sequences to GenBank. (Fig. 1C, D).

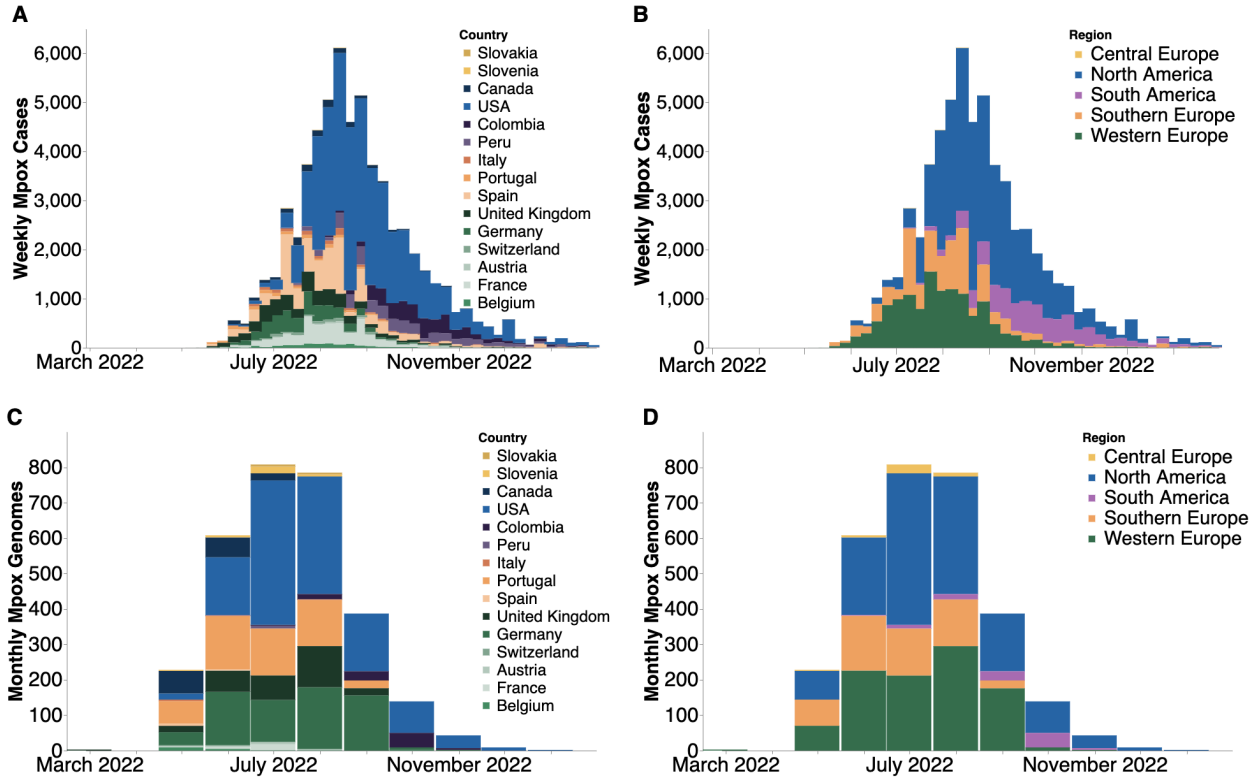

Fig. 1. Case counts and publicly available sequences by geographic region. (**A, B**) Confirmed positive weekly mpox cases by country (**A**) and global region (**B**) smoothed using a 7 day rolling average on daily data and then aggregating into weekly counts. Only countries with greater than 5 sequences on GenBank were included. (**C, D**) Monthly count of publicly-available MPXV genomes found on GenBank by country (**C**) and global region (**D**).

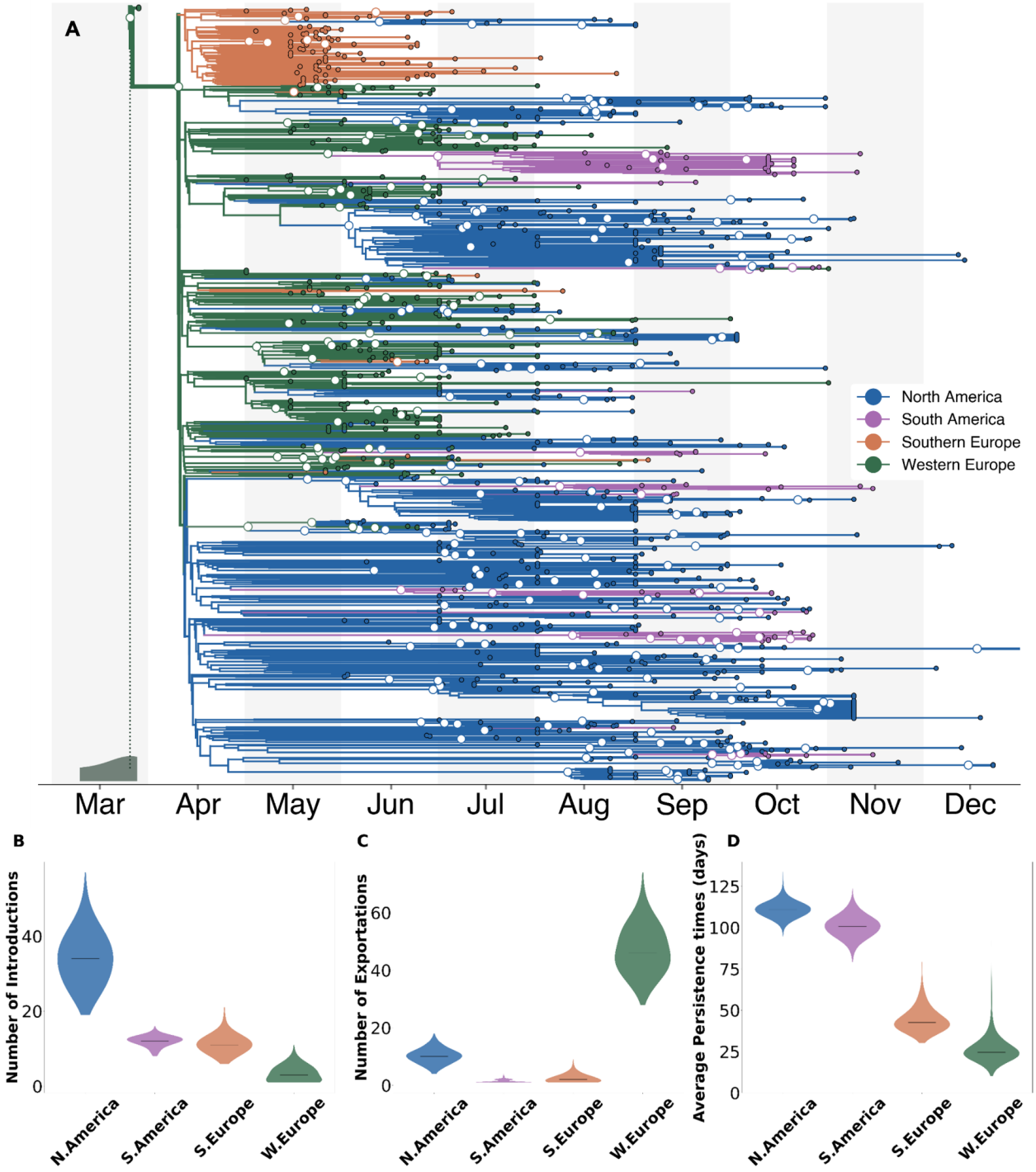

Fig. 2. Phylogeographical estimates of MPXV spread in 4 global regions. (**A**) The maximum clade credibility tree summary of the Bayesian inference conducted using asymmetric discrete trait analysis and Skygrid prior on 1004 sequences. Colors correspond to the regions in the legend. Ancestral nodes with greater than 50% posterior support are highlighted with a white circle overlaid. Inset histogram on bottom left corner shows 95% interval for the time to most recent common ancestor (TMRCA)(**B-D**) Estimated number of introductions (**B**), exports (**C**), and average time of local persistence in days (**D**) for each global region. Horizontal black line denotes median estimates.

To investigate the spread of mpox throughout the course of the epidemic across global regions, we employed a phylogeographic approach with an asymmetrical discrete trait model on 1004 publicly available MPXV sequences subsampled based on confirmed case counts (Fig. 2). We chose a case count weighted subsampling scheme since discrete trait analysis assumes that sample sizes across subpopulations are proportional to their relative population prevalence (49). Due to the low number of recorded cases in Central Europe, no sequences from that region were included in the final subset (Supp. Fig 1). We infer that the most recent common ancestor (MRCA) of the epidemic existed between March 9th and March 27th, 2022 (95% HPD) and phylogeographic estimation assigns this ancestor to Western Europe. However, alternative phylodynamic models place the MRCA in November or December 2021 (Supp. Table 2). We infer the evolutionary clock rate to be 8.41×10^{-5} (95% HPD 7.71×10^{-5} to 9.10×10^{-5}) substitutions per site per year or approximately 16.6 substitutions per genome per year.

We observe strong population structure where single introductions often result in large local clades. These large local clades suggest that local spread played a considerable role in their respective regional outbreaks. We find rapid early spread in Western Europe lead to a high number of introductions to other global regions (46 introduction events, IQR: 41-53), seeding regional outbreaks (Fig. 2C). Our findings also show evidence of repeated dissemination into North America and subsequent sustained community transmission as North America had the highest median number of viral importations and longest median viral persistence time (111 days, IQR: 108-114) (Fig. 2B,D).

To test the appropriateness and accuracy of the phylogeographic inference, we repeated the analysis in which 10% (100 tips in total) of the sequence locations were masked. We then inferred these locations via the same phylogeographic approach and found that the model correctly inferred 93% of the masked tip locations, suggesting a strong genomic signal (Supp Fig. 2).

Rapid early spread characterized by significant underdetection of cases

In order to analyze within-region transmission dynamics, improve robustness to sampling bias, and enhance inference via the joint integration of genomic and epidemiological metadata, we then employed an approximate structured coalescent (MASCOT) with a generalized linear model (GLM) approach with estimated prevalence and air passenger data as empirical predictors on 587 sequences (Supp. Fig 3). We also included a predictor for each month within the time period studied to account for potential changes in case detection over time. The included sequences were subsampled with equal temporal weighting to increase representation of undersampled regions such as Central Europe (Supp Fig. 1**)**. The MASCOT-GLM subsampling scheme is different from the subsampling for the DTA analysis as the structured coalescent is more robust to differences in sampling across regions and is subsequently informed by regional prevalence (49,50). We used a GLM approach in order to draw inferential power from relevant predictors

and reduce uncertainty relative to inferences using the coalescent alone. After separating out each introduction and its inferred descendents from the maximum clade credibility tree and comparing them to confirmed case counts, we see strong evidence of viral circulation before initial detection in each global region (Fig 3A). Additionally, we revealed that the largest downstream outbreak clusters arise from introductions prior to detection from public health surveillance while introductions after detection are more likely to be a single case and extinguish quickly (Supp. Fig. 5).

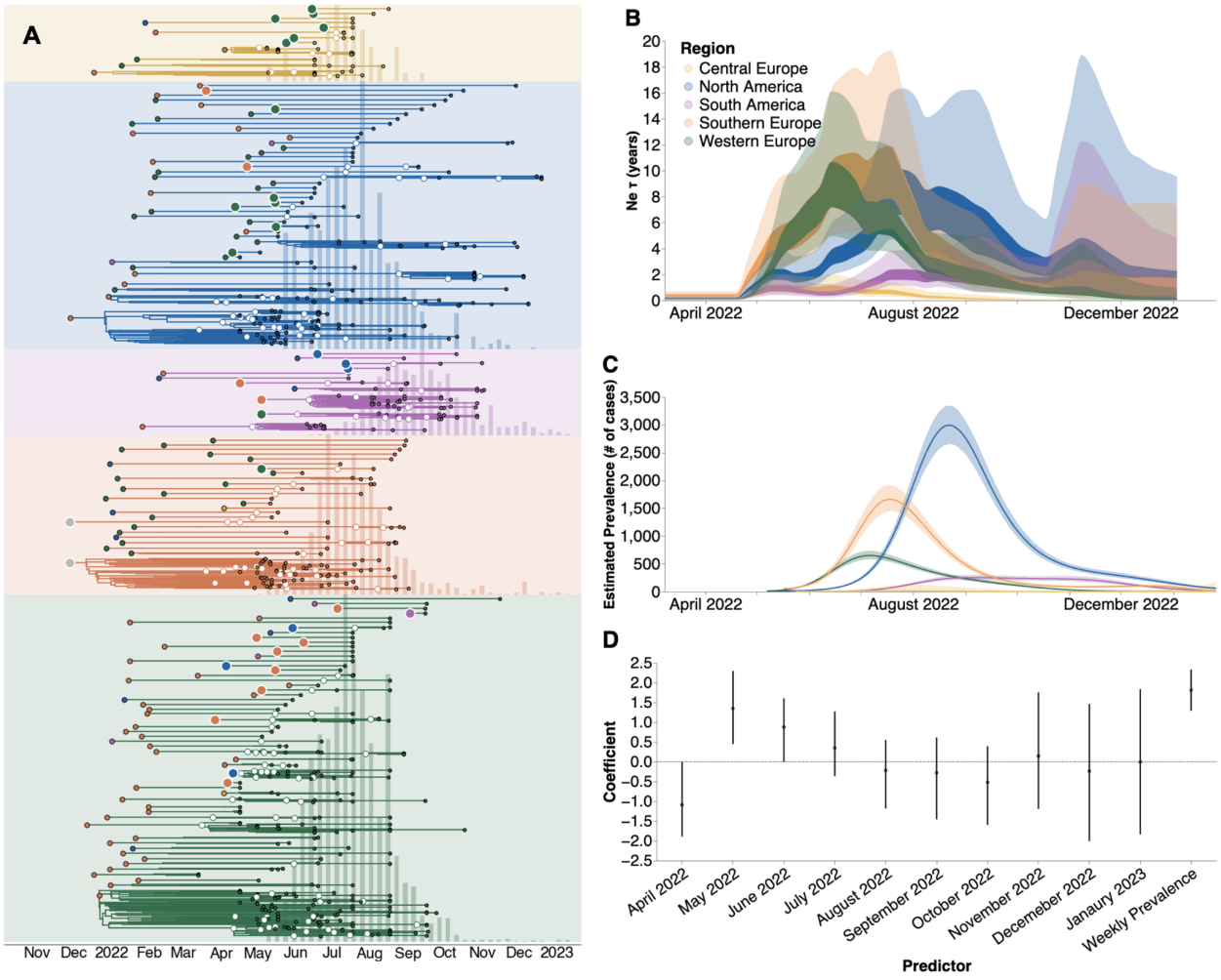

Fig. 3. Phylodynamic investigation reveals underdetection of mpox. (**A**) Regional specific introductions and the resulting outbreak clusters extracted from the maximum clade credibility tree summary of the Bayesian inference conducted using MASCOT-GLM on 587 sequences. Colors correspond to the regions in the legend. Ancestral nodes with greater than 50% posterior support are highlighted with a white circle overlaid. (**B**) Estimates of effective population sizes ($Ne\tau$ in years) from April 2022 through December 2024 using 550 sequences subsampled equally throughout time. (**C**) Regional prevalence (in number of cases, interpreted as census population size N) estimated

independently using publicly-available case counts, and (**D**) Estimates of model predictor coefficients for *Ne* estimation. Dark line represents median estimates, light bands represent 95% HPD.

We sought to investigate the extent of underdetection in each region by comparing the MASCOT-GLM estimates of effective population size *Ne* (Fig. 3B) with the prevalence estimated solely from case counts (Fig. 3C), which we assume to approximate the census population size. Of note, the MASCOT-GLM estimates are informed by prevalence as an empirical predictor, allowing us to assume that differences between the coalescent-derived *Ne* and case-based prevalence estimates could be due to differential case reporting. While both estimates show regional peaks at similar points in time, we find a divergence between the two estimates in the early months of the outbreak – May, June, July 2022 – where our coalescent-derived *Ne* show continuous viral epidemic growth before case-based prevalence counts report any cases detected by local public health authorities, suggesting significant underdetection of cases in these months. This observation is supported by the estimated coefficients of the monthly predictors that show the direction and magnitude of each predictor's effect on the inference of regional *Ne.* Figure 3D shows that the predictors for the months of May, June, and July 2022 had a strong positive effect on predicting regional *Ne.* By August 2022, however, when a substantial number of cases had been detected in all five regions, we see that our model no longer finds the monthly predictors to be required, implying that prevalence estimates are sufficient to describe *Ne*. The strong positive effect of the monthly predictors from May through July, even in the presence of competing information from the prevalence predictor, suggests significant underreporting of cases in these first few months. For comparison with our predictor-informed MASCOT-GLM model, a strictly coalescent-based model (Supp. Fig. 4) shows similar trends in *Ne* but displays a larger degree of uncertainty, supporting the use of empirical predictors to inform our inference.

After initial dissemination, viral importations had limited impact on local spread

When analyzing transmission chains resulting from introductions (Fig. 3A), we identified a bimodal pattern in each region, where most viral introductions resulted in a single imported case while a very small number of introductions spark explosive and widespread local transmission. Upon identifying the regional introductions with the highest posterior support in our MCC tree, we find that introductions that occurred early in the global outbreak lead to larger and more persistent transmission chains, while those introductions that occurred after initial public health detection in each region resulted in smaller outbreaks that extinguished faster (Fig. 4A, Supp. Fig. 5). We also found that air passenger volumes between each global region were a significant positive predictor of viral migration between each region, highlighting the importance of regional connectivity in promoting international viral spread (Fig. 4B).

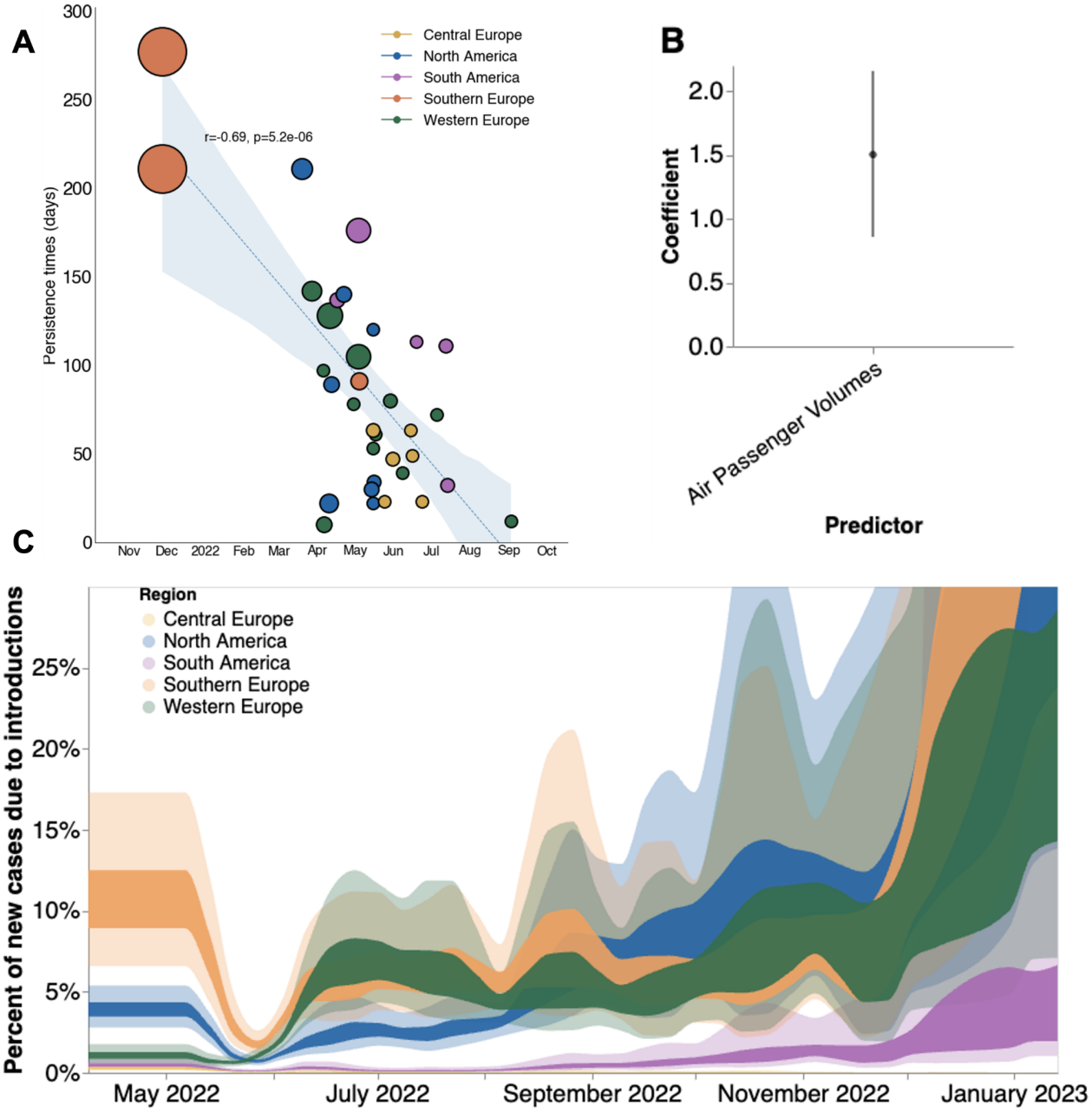

Fig. 4. Phylodynamic estimates of MPXV transmission dynamics in 4 global regions. (**A**) Relationship between estimated date of introduction and persistence time**.** Each circle represents a single viral introduction with greater than 50% posterior support into the region denoted by the color (i.e. a green point represents an introduction into Western Europe). The size of each point is proportional to the size of the outbreak cluster resulting from each introduction with larger circles representing more resulting downstream tips. Blue dashed line represents the linear best fit line using Pearson's correlation. Blue shaded region denotes the variability of the line and the resulting estimates from Pearson's correlation are shown in text above the shaded region. (**B)** Estimates of model predictor coefficients for migration rate estimation. (**C**) Percentages of new cases due to introductions were estimated as the relative contribution of introductions to the overall number of infections in the region. The inner area denotes the 50% HPD interval and the outer area denotes the 95% HPD interval

We sought to estimate the relative contribution of introductions versus local community spread in driving the epidemic in each global region via inferred parameters from MASCOT-GLM. To quantify the impact of those introductions, we calculated the percentage of new cases from introductions in each region using the estimated changes in *Ne* over time, the rate of viral migration between regions, and the incubation and infectious periods distributions for mpox. We found that introductions played a relatively small role in each regional epidemic, with introductions resulting in an average of 1.5-10% of new cases over the time period studied (Fig. 4C). We see that the percentage of new cases due to introductions is lowest from June to August 2022, when most regions were experiencing the peak of their respective epidemics. We also see large variability in the contribution of introductions on local spread during the later months which could be driven by lack of genomic and case-based information at those time periods (Fig. 3D).

To better understand transmission dynamics locally within each region, we computed *Rt*, the time-varying effective reproductive number, using the estimated growth rate derived from changes in effective population size (Fig. 5). We also employed our estimates of the percentage of new cases that are due to introductions to calculate *Rt* without the influence of introductions (Supp Fig. 6). Initially, we observe high *Rt* with viral establishment in each respective region followed by a subsequent rapid decrease in which most regions achieve $Rt < 1$ (signaling an declining epidemic) by September 2022. Removing the contribution of introductions, however, has a very small effect on regional *Rt,* showing the limited impact of introductions on local viral spread after initial regional establishment (Supp. Fig 6).

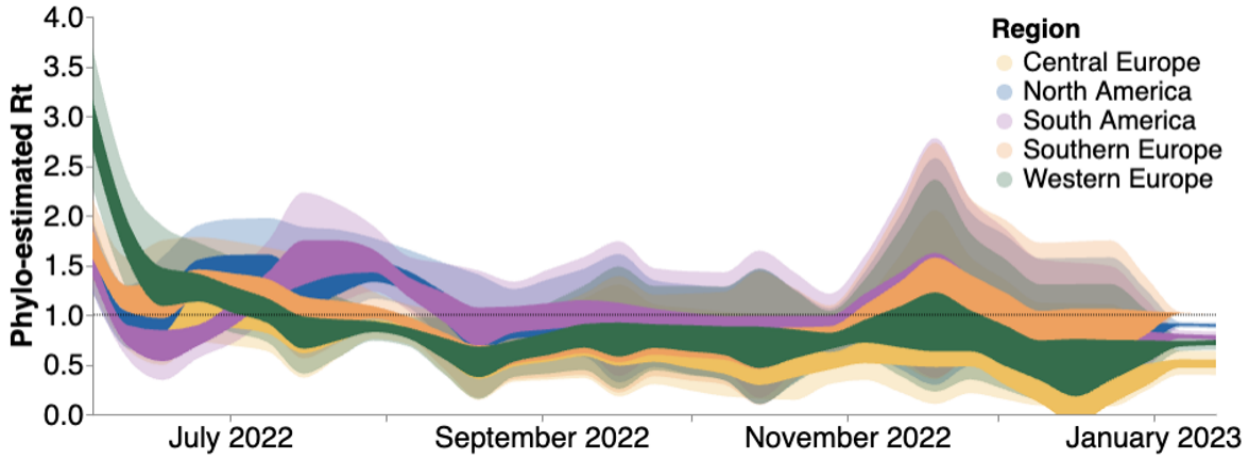

Figure 5: Estimates of time-varying reproductive number (*Rt*) in five global regions. Estimates of *Rt* from April 2022 through December 2023 via MASCOT-GLM using 587 sequences subsampled equally throughout time. The inner area denotes the 50% HPD interval and the outer area denotes the 95% HPD interval. Dashed line highlights an *Rt* value of 1 above which denotes an exponentially growing viral epidemic.

US vaccine campaigns had limited impact on curbing the North American outbreak

Given that North America bore the highest burden of mpox cases throughout the epidemic, we focused on this region to explore the role introductions had on prolonging the local epidemic as well as the impact of mpox vaccination on *Rt*. We find that introductions accounted for only an average of about 5-10% of local spread. By focusing on the declining half of the North American epidemic (dates laters than June 15, 2022), we additionally found that preventing introductions following the initial seeding event would have caused the *Rt* to fall below one only less than a week earlier (Supp. Fig. 6), highlighting the relatively low importance of introductions.

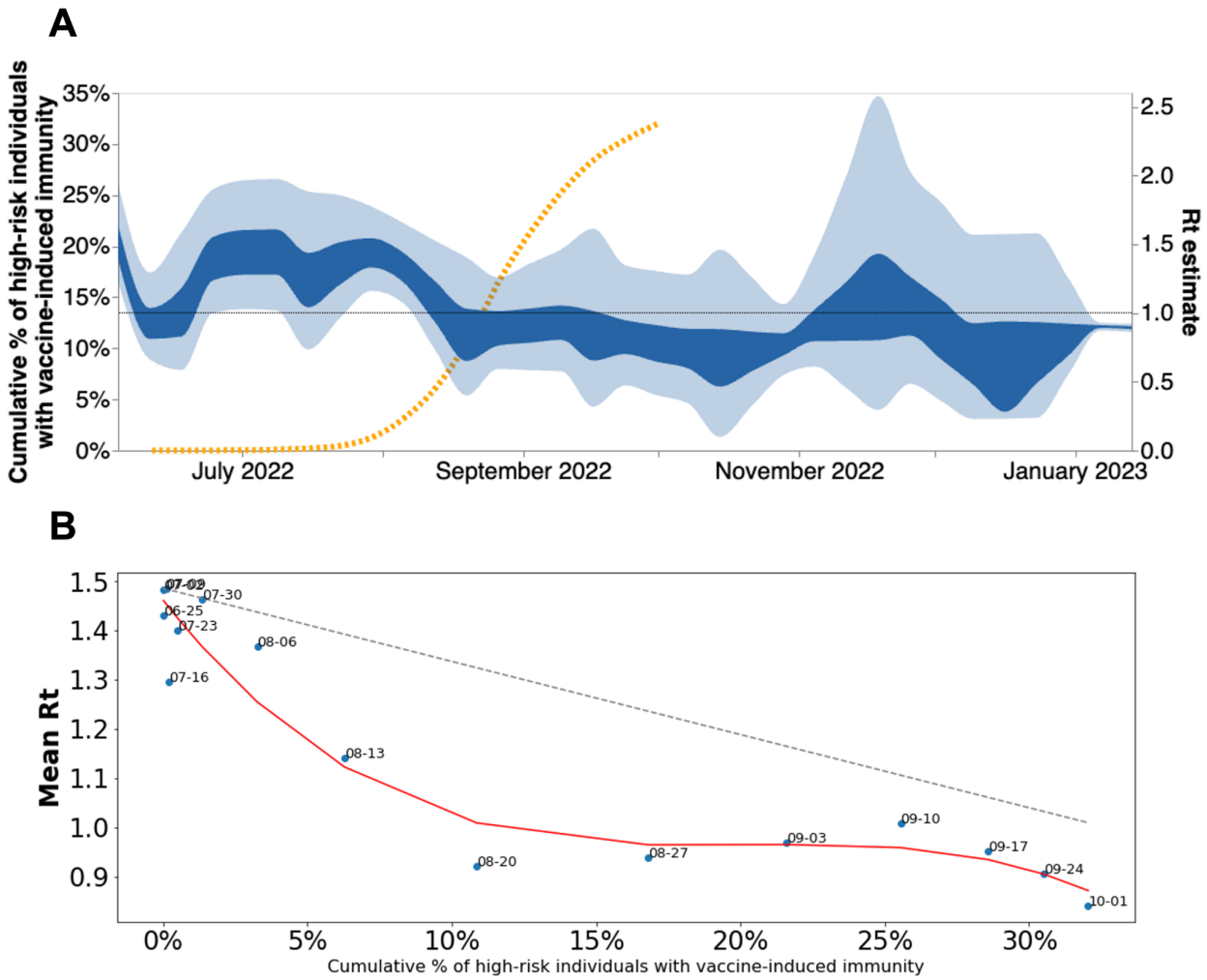

Fig. 6. North American MPXV local transmission dynamics. (**A**) North American *Rt* estimated via phylodynamics (solid bands). Dashed orange line indicates the cumulative percentage of high-risk individuals with vaccine-induced immunity in the US. (**B**) Scatter plot comparing mean *Rt* calculated via MASCOT-GLM for North America vs cumulative percentage of high risk individuals with vaccine-induced immunity in the United States. Red line indicates the best fit spline for scattered points. Dashed grey line indicates expected linear decrease in *Rt* with increasing vaccine-immunity assuming SIR dynamics.

When we overlaid North American *Rt* estimates alongside the cumulative percentage of high-risk individuals in the USA with mpox vaccine-derived immunity, we found that *Rt* began declining prior to initiation of vaccination in the US (Fig. 6A). North American *Rt* estimates fell below one near the middle of August 2022, when the cumulative percentage of high-risk individuals with vaccine-derived immunity was less than 8%. Under an SIR model of infectious disease dynamics, vaccine-derived immunity impacts disease transmission by removing individuals from the susceptible population in a linear fashion. Before there was any mpox vaccine-derived immunity in the US, North American *Rt* peaked at 1.49. Assuming a linear decrease in *Rt* as cumulative vaccine-derived immunity increased, we would expect *Rt* to fall below 1 only after greater than 33% of the high-risk population of the US developed immunity against mpox (Fig. 6B, dashed grey line). When we compare the actual decay of *Rt* in North America, we find that *Rt* falls below one before about 10% of the high risk population developed immunity (Fig. 6B, blue scatter points and red spline), implying that vaccination is not primarily responsible for the drop of *Rt* below 1. Of note, we were only able to publicly access vaccination information for the US via the CDC but our regional *Rt* analysis for North America includes viral dynamics for both the US and Canada.

High degree of transmission heterogeneity observed in the declining phase of the mpox epidemic

Upon separating out each introduction and its inferred descendents from the maximum clade credibility tree (Fig. 3A), we noticed that a small number of introductions resulted in a sustained expansion of local transmission while the remaining majority of introductions produced few downstream infections. We sought to quantify mpox transmission heterogeneity by analyzing the size distribution of clusters of identical sequences (46).

We observed that the mean size of clusters of identical sequences decreased over the course of the epidemic (Fig. 7A). We found that the timing of the decrease across locations was consistent with our estimates of *Rt* obtained from the analysis of case and sequence data (Fig. 5), with larger cluster sizes observed in the US than in Europe during June 2022. Globally, the size of clusters of identical sequences ranged from 1 to 118 with 61% of sequences belonging to a cluster of size greater than 1 (Supp. Fig. 8). The probability to observe a cluster of a given size is determined by the effective reproduction number *R* across the period, the degree of transmission heterogeneity measured by the dispersion parameter *k* and the fraction of infections sequenced (see Methods). Figure 7B depicts how the probability to observe a cluster of size 118 (knowing we observed 2624 clusters) is impacted by *R* and *k* assuming that 5.5% of infections were sequenced (average proportion of cases sequenced throughout the epidemic). We find that for values of the reproduction number *R* greater than 1.5, observing a cluster of identical sequences of size 118 is not unlikely regardless of the value of the dispersion parameter *k*. This is consistent with the fact that in this parameter regime, the expected mean number of offspring with identical genomes is greater than 1 so that we expect some clusters of identical sequences to not go extinct (47). For a value of the dispersion parameter similar to what has been estimated during previous

mpox outbreaks (e.g. 0.36 in (51)), the reproduction number would need to be greater than 1.31 for this probability to reach 5%. Considering a lower dispersion parameter value (0.1 which is on the lower range of what has been estimated across different pathogens (48)) would still require the reproduction number to be greater than 1.21 for this probability to reach 5%. This suggests that transmission heterogeneity alone (without a reproduction number greater than 1) is unlikely to explain the size of the large polytomy observed at the beginning of the epidemic.

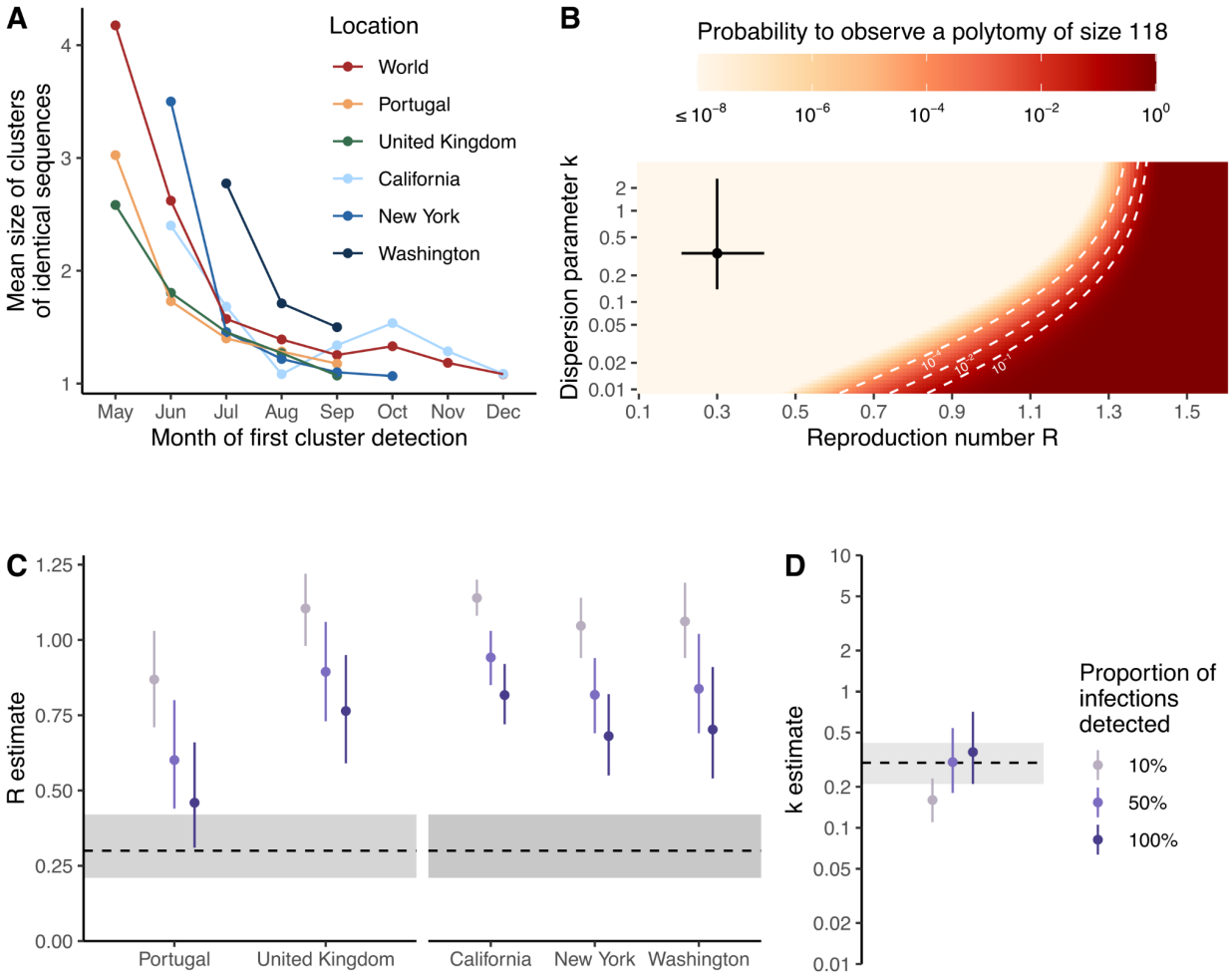

Fig. 7. Transmission heterogeneity estimates obtained from clusters of identical mpox sequences. **(A)** Mean size of clusters of identical sequences for different geographical regions by month of first cluster detection. **(B)** Probability to observe a cluster of size 118 among 2624 clusters as a function of the reproduction number *R* and the dispersion parameter *k* assuming 5.5% of infections are sequenced. Estimates of **(C)** the reproduction number *R* by geographical unit and **(D)** the dispersion parameter *k* across geographical units from August 2022 exploring different assumptions regarding the proportion of infections detected. In B, the point corresponds to estimates obtained by Blumberg and Lloyd-Smith (43) from the analysis of epidemiological clusters during previous outbreaks. The segments correspond to the associated 95% confidence intervals. In C-D, points correspond to maximum likelihood estimates and vertical segments to 95% likelihood profile confidence intervals. The horizontal dotted line and the

shaded area correspond to estimates obtained by Blumberg and Lloyd-Smith (43) from the analysis of epidemiological clusters during previous outbreaks. In B, the dotted white lines correspond to contour lines for probabilities of 10^{-4}, 10^{-2} and 10^{-1}.

We then estimated *R* and *k* during the decreasing phase of the epidemic in different geographical regions (Fig. 7C-D, Supp. Tables 3-4). Assuming that half of infections were detected, we estimated *k* across locations at 0.30 (95% CI: 0.18-0.54) and reproduction numbers below unity across locations (Supp. Table 3). This corresponds to heterogeneity in transmission with 65% - 72% of infected individuals producing 0 offspring (and hence the remainder responsible for all transmission events). Assuming a greater fraction of infections were detected lead to lower estimates of *R* and greater estimates of *k*. This had however little impact on the fraction of individuals producing 0 offspring (Supp. Table 3). Allowing the dispersion parameter *k* to vary between locations resulted in similar estimates, though with considerably more uncertainty (Supp. Table 4). Our results suggest considerable transmission heterogeneity which could be explained by the structure of the sexual contact network in MSM (52,53). Our estimate is consistent with those previously obtained for sexually-transmitted infections spread between MSM (e.g. dispersion parameter of 0.257 estimated during a gonorrhea outbreak in MSM (54)).

Discussion

Despite the heightened focus on public health surveillance of emerging infections since the start of the SARS-CoV-2 pandemic, MPXV sparked regional epidemics around the world, contributing to a high degree of morbidity among those affected (52,55,56). In this study, we present both a global and regional view of mpox detection, expansion, and containment by jointly analyzing genomic, mobility, and epidemiological data. We find evidence of explosive spread following initial regional viral seeding events, community transmission prior to detection by local public health surveillance, differential changes in case-detection throughout the epidemic, a limited role of viral introductions in prolonging regional epidemics, a large degree of transmission heterogeneity, and limited impact of vaccination during the early phases of the North American epidemic.

While prior studies have analyzed the global spread of MPXV via phylogenetic methods (13–15), they were often limited by small sample sizes and a superficial description of regional trends. Recent advances in phylodynamic and phylogenetic methods have been developed to tackle issues of low genetic diversity, as found in mpox, where phylodynamic uncertainty is reduced by the joint inference of genomic information alongside relevant predictors, such as epidemiological and mobility information (36,43,53,57). In the present study, we leverage these recent advances through the use of MASCOT-GLM, an approximate structured coalescent approach found to be more robust to sampling bias than traditional phylogeographic methods that allows for the integration of important predictors, notably case counts and air passenger volumes, to inform estimates of local transmission dynamics and regional viral migration.

These phylodynamic estimates, in addition to untangling global dispersion, allow us to explore changes in case detection and the impact of viral introductions on local spread on a regional level, highlighting global differences in epidemic outcomes. Despite the heightened interest in public health surveillance, we found evidence of early undetected spread in each region (Fig. 3). These early undetected transmission events were often associated with the largest downstream clusters, while later viral introductions were quickly contained. Additionally, we found a strong influence of monthly predictors for the beginning months of the epidemic – May, June, July 2022 – with regards to estimating regional effective population size. The strong effect of the early monthly predictors implies the presence of significant case underreporting as the prevalence predictor in our model was not solely sufficient to inform inference of *Ne.* Despite worldwide attempts to improve public health surveillance, our study shows the limitations of current surveillance systems, promoting the need for broader routine specimen screening for a wide range of pathogens with outbreak potential.

An outstanding question raised during the beginning of the mpox epidemic that remains unclear is the potential impact of interventions in preventing and controlling spread (58). Similar to the early phases of the SARS-CoV-2 pandemic, the MPXV epidemic prompted considerations around travel bans and restrictions in an attempt to curb transmission to previously unaffected areas. While travel bans were ultimately not implemented, the CDC issued a series of travel recommendations and warnings for both individuals exposed to MPXV and for those traveling to areas with a high number of mpox cases on June 6, 2022 (59). Despite these travel recommendations, our models show that there were already many introduced lineages circulating in North America before June 6th (Fig. 3), limiting the impact and effectiveness of these recommendations on curbing disease spread. Our results show that following initial viral seeding, viral introductions played a limited role in promoting local transmission, accounting for less than 10% of new cases in any given region studied (Fig. 4). We also found that removing the influence of introductions also would have had limited impact in the timing of North American *Rt* dropping below one (Supp. Fig. 6). Together this suggests little potential impact of travel restrictions after mid-May 2022 once MPXV had already been established in the region. Our estimates of transmission heterogeneity, where we found that only 28-35% of infected individuals were responsible for all transmission events observed during the decreasing phase of the epidemic (Fig. 7), promotes tailoring public health interventions to high risk groups rather than population-wide policies.

We also examined the potential impact of vaccination on controlling the mpox epidemic in North America by comparing changes in local transmission as measured by *Rt* to the cumulative percentage of high-risk individuals in the US with vaccine-derived immunity (Fig. 6). While even a half vaccination dose has been found to be effective at providing robust immunity against mpox (60,61), there was concern over the delayed start of vaccination in the US. We find that local transmission in North America decreased below one (which denotes a declining epidemic)

before 10% of the population had any vaccine-induced immunity. Our conclusions are concordant with those from the the CDC which also found that *Rt* fell below one in August 2022 and they calculate that at their estimated time point only about 1.3% of the population at high risk for mpox in the US had any vaccine-induced immunity (22), suggesting that vaccination alone cannot wholly explain the drop in mpox transmission. Differences in the timing of *Rt* falling below one could be due to a difference in methodology as the CDC estimates relied solely on captured cases reported to the CDC. Similarly, modeling studies have found that behavioral modifications within the queer community was the main contributing factor to the slowing mpox spread in Washington D.C., although they also found that vaccination was ultimately needed to definitively curb the local epidemic (62,63). Additionally, a UK-based modeling study focusing on gay and bisexual men who have sex with men found that vaccination could not explain the drop in mpox incidence in the region, but rather attribute the declining incidence to changes in behavior within the same community (64). Together, these findings highlight the significant effect of behavioral change among men who have sex with men and other high-risk communities in curbing the epidemic as well as push for a prompt public health response that includes early vaccination campaigns in order to maximize the population-level effectiveness of vaccines.

Our study has noteworthy limitations. Our genomic data only cover a small selection of countries and regions, suggesting that we are missing transmission events that involve unsampled countries, especially from regions such as Asia, Oceania, and Africa. Additionally, the changing availability of genomic sequencing, as well as unequal sampling across the regions study affect the probability that a case shows up as a sequence in our dataset through the period studied. We attempted to account for this variation by weighting the subsampling for our phylogeographic (DTA) analysis according to confirmed case counts, and by oversampling undersampled regions (and downsampling overrepresented regions) in our MASCOT-GLM analysis (Supp. Fig. 1) as well as by adding in case counts as an empirical predictor in the model in an effort to account for this variation.

Additionally, Bayesian coalescent models assume random sampling of infected individuals, meaning that targeted sampling of super spreader events, or via contact tracing, could bias our phylodynamic estimations. We attempt to quantify the extent of transmission heterogeneity via our estimates of overdispersion (Fig. 7). Additionally, given the discrepancy of the TMRCA between our two models (Supp. Table 2), we find our TMRCA calculations to be highly dependent on the tree prior and thus should be interpreted with caution, although given the integration of various data streams, we believe the MASCOT-GLM results to be more plausible. Lastly, our *Rt* calculations assume that the change in *Ne* over time is proportional to the change in the number of infected individuals over time. Despite the potential violation of the panmixia assumption, we estimated *Rt* and the number of imports over time using methods independent of our phylodynamic models and found highly congruent results, supporting the validity of our results (Figs. 4, 5).

In conclusion, our study integrates diverse data streams to provide novel insights on the spread and control of mpox. Despite the global efforts in augmenting genomic and traditional public health surveillance, our study shows a high degree of underdetection of cases in the early stages of the epidemic which contributed to rapid community spread. We demonstrate that the vaccination campaigns in the US had limited impact on curbing the rapid transmission observed in the summer of 2022, highlighting the impact of behavioral changes within the MSM community. Our findings are relevant for policymakers in promoting broader routine specimen screening as a core tenant of pandemic preparedness. Recent emerging disease outbreaks – Zika, Ebola, SARS-CoV-2, and now mpox – have been characterized by late public health detection and cryptic local transmission as a result (31,65,66). Our work shows that rapid pathogen detection and subsequent behavioral change could be sufficient to curb epidemic spread. Additionally, our work prompts swift public health investments and interventions to protect marginalized and vulnerable populations from mpox and other emerging infections (11,56).

Funding

MIP and MF are ARCS Foundation scholars. MF was supported by the National Science Foundation Graduate Research Fellowship Program under Grant No. DGE1762114. T.B. is a Howard Hughes Medical Institute Investigator. This work was supported by NIH NIGMS award R35 GM119774 to T.B. Analyses were completed using Fred Hutch Scientific Computing resources (NIH grants S10-OD-020069 and S10-OD-028685).

Acknowledgments

We would like to thank Allison Black for constructive feedback, discussions, and edits. We gratefully acknowledge all data contributors, i.e. the Authors and their Originating laboratories responsible for obtaining the specimens, and their Submitting laboratories for generating the genetic sequence and metadata and sharing via GenBank. The laboratories and institutions that contributed more than ten sequences for this study are as follows: Los Angeles County Public Health Laboratories, Los Angeles County Department of Public Health, UW Virology, Laboratory Medicine, UKHSA, Research and Evaluation, CDC, DHCPP-PRB, Robert Koch Institute, Centre for Biological Threats, Highly Pathogenic Viruses, National Institute of Health Doutor Ricardo Jorge, Portugal (INSA), Department of Infectious Diseases, Laboratorio Departamental de Salud Publica de Antioquia, Antioquia, Instituto Nacional de Salud, Direccion de Investigacion en Salud Publica, National Microbiology Laboratory, Public Health Agency of Canada, Institute National de Saude Doutor Ricardo Jorge (INSA), Portugal, CDPH, VRDL, IHU - Mediterranee Infection, MEPHI, Centre for Biological Threats, Highly Pathogenic Viruses, Robert Koch Institute, Germany, New Jersey Department of Health, Public Health and Environmental Laboratories, Rush University Meical Center, Regional Innovative Public Health Laboratory (RIPHL), University of Nebraska Medical Center, Environmental, Agricultural, and Occupational Health, Universidad Tecnologica de Pereira, Laboratorio de Biologia Molecular y Biotecnologia / Facultad de ciencias de la salud, Royal Infirmary of Edinburgh, Viral Genotyping

Reference Laboratory, Institute of Microbiology and Immunology, Faculty of Medicine, University of Ljubljana, Laboratory for Diagnostics of Zoonoses and WHO Centre, Institute of Tropica Medicine, Department of Clinical Sciences, Medical University of Vienna, Center for Virology, Instituto Nacional de Salud Peru, Laboratorio de Biotecnologia y Biologia Molecular. We have included a detailed acknowledgements table in Supplementary Data.

Declaration of interests

All authors declare no competing interests.

Author Contributions

Conceived and designed the study: MIP, NA, TB
Curated the data: MIP, NA, VC, CTK
Conducted the analysis: MIP, NA, MF, VC, CTK, NFM
Advised on analysis: VC, PL, JTM, TB
Drafted the manuscript: MIP, NA, MF, NFM, CTK
Reviewed and edited the manuscript: All authors

Ethics Approval

All data used in this study is publicly available, suitably anonymized viral sequence data. As such it does not constitute human-subjects research.

Data Availability

Nextstrain builds, BEAST XMLS, scripts, sequence information, and de-identified data can be found at https://github.com/blab/mpox-dynamics. All sequences are available on GenBank with accession numbers found in the supplementary information.

References:

1. Huang Y, Mu L, Wang W. Monkeypox: epidemiology, pathogenesis, treatment and prevention. Signal Transduct Target Ther. 2022 Nov 2;7(1):1–22.
2. Lum FM, Torres-Ruesta A, Tay MZ, Lin RTP, Lye DC, Rénia L, et al. Monkeypox: disease epidemiology, host immunity and clinical interventions. Nat Rev Immunol. 2022 Oct;22(10):597–613.
3. Thornhill JP, Barkati S, Walmsley S, Rockstroh J, Antinori A, Harrison LB, et al. Monkeypox Virus Infection in Humans across 16 Countries — April–June 2022. N Engl J Med. 2022 Aug 25;387(8):679–91.
4. CDC. Centers for Disease Control and Prevention. 2023 [cited 2023 Apr 19]. Mpox in the U.S. Available from: https://www.cdc.gov/poxvirus/mpox/images/monkeypox.jpg
5. Petersen E, Kantele A, Koopmans M, Asogun D, Yinka-Ogunleye A, Ihekweazu C, et al. Human Monkeypox: Epidemiologic and Clinical Characteristics, Diagnosis, and Prevention. Infect Dis Clin North Am. 2019 Dec 1;33(4):1027–43.
6. Guzzetta G, Mammone A, Ferraro F, Caraglia A, Rapiti A, Marziano V, et al. Early Estimates of Monkeypox Incubation Period, Generation Time, and Reproduction Number,

Italy, May–June 2022 - Volume 28, Number 10—October 2022 - Emerging Infectious Diseases journal - CDC. [cited 2023 Apr 19]; Available from: https://wwwnc.cdc.gov/eid/article/28/10/22-1126_article

7. De Baetselier I, Van Dijck C, Kenyon C, Coppens J, Michiels J, de Block T, et al. Retrospective detection of asymptomatic monkeypox virus infections among male sexual health clinic attendees in Belgium. Nat Med. 2022 Nov;28(11):2288–92.
8. Fleischauer AT, Kile JC, Davidson M, Fischer M, Karem KL, Teclaw R, et al. Evaluation of Human-to-Human Transmission of Monkeypox from Infected Patients to Health Care Workers. Clin Infect Dis. 2005 Mar 1;40(5):689–94.
9. Guagliardo SAJ, Monroe B, Moundjoa C, Athanase A, Okpu G, Burgado J, et al. Asymptomatic Orthopoxvirus Circulation in Humans in the Wake of a Monkeypox Outbreak among Chimpanzees in Cameroon. Am J Trop Med Hyg. 2019 Nov 25;102(1):206–12.
10. WHO Director-General's statement at the press conference following IHR Emergency Committee regarding the multi-country outbreak of monkeypox - 23 July 2022 [Internet]. [cited 2023 Apr 19]. Available from: https://www.who.int/director-general/speeches/detail/who-director-general-s-statement-on-the-press-conference-following-IHR-emergency-committee-regarding-the-multi--country-outbreak-of-monkeypox--23-july-2022
11. Gonsalves GS, Mayer K, Beyrer C. Déjà vu All Over Again? Emergent Monkeypox, Delayed Responses, and Stigmatized Populations. J Urban Health. 2022 Aug 1;99(4):603–6.
12. Volz EM, Koelle K, Bedford T. Viral Phylodynamics. PLOS Comput Biol. 2013 Mar 21;9(3):e1002947.
13. Patiño LH, Guerra S, Muñoz M, Luna N, Farrugia K, van de Guchte A, et al. Phylogenetic landscape of Monkeypox Virus (MPV) during the early outbreak in New York City, 2022. Emerg Microbes Infect. 2023 Dec 31;12(1):e2192830.
14. Gao L, Shi Q, Dong X, Wang M, Liu Z, Li Z. Mpox, Caused by the MPXV of the Clade IIb Lineage, Goes Global. Trop Med Infect Dis. 2023 Feb;8(2):76.
15. Gigante CM, Korber B, Seabolt MH, Wilkins K, Davidson W, Rao AK, et al. Multiple lineages of monkeypox virus detected in the United States, 2021–2022. Science. 2022 Nov 4;378(6619):560–5.
16. Isidro J, Borges V, Pinto M, Sobral D, Santos JD, Nunes A, et al. Phylogenomic characterization and signs of microevolution in the 2022 multi-country outbreak of monkeypox virus. Nat Med. 2022 Aug;28(8):1569–72.
17. Aksamentov I, Roemer C, Hodcroft EB, Neher RA. Nextclade: clade assignment, mutation calling and quality control for viral genomes. J Open Source Softw. 2021 Nov 30;6(67):3773.
18. O'Toole Á, Neher RA, Ndodo N, Borges V, Gannon B, Gomes JP, et al. Putative APOBEC3 deaminase editing in MPXV as evidence for sustained human transmission since at least 2016 [Internet]. bioRxiv; 2023 [cited 2023 Apr 19]. p. 2023.01.23.525187. Available from: https://www.biorxiv.org/content/10.1101/2023.01.23.525187v1
19. Hadfield J, Megill C, Bell SM, Huddleston J, Potter B, Callender C, et al. Nextstrain: real-time tracking of pathogen evolution. Bioinformatics. 2018 Dec 1;34(23):4121–3.
20. Minh BQ, Schmidt HA, Chernomor O, Schrempf D, Woodhams MD, von Haeseler A, et al. IQ-TREE 2: New Models and Efficient Methods for Phylogenetic Inference in the Genomic Era. Mol Biol Evol. 2020 May 1;37(5):1530–4.
21. Sagulenko P, Puller V, Neher RA. TreeTime: Maximum-likelihood phylodynamic analysis.

Virus Evol. 2018 Jan 8;4(1):vex042.
22. CDC. Centers for Disease Control and Prevention. 2023 [cited 2023 Apr 19]. Monkeypox Technical Reports. Available from: https://www.cdc.gov/poxvirus/mpox/cases-data/technical-report/report-3.html
23. Gilbert M, Pullano G, Pinotti F, Valdano E, Poletto C, Boëlle PY, et al. Preparedness and vulnerability of African countries against importations of COVID-19: a modelling study. The Lancet. 2020 Mar 14;395(10227):871–7.
24. Page AJ, Taylor B, Delaney AJ, Soares J, Seemann T, Keane JA, et al. SNP-sites: rapid efficient extraction of SNPs from multi-FASTA alignments. Microb Genomics. 2016 Apr;2(4):e000056.
25. Danecek P, Bonfield JK, Liddle J, Marshall J, Ohan V, Pollard MO, et al. Twelve years of SAMtools and BCFtools. GigaScience. 2021 Feb 1;10(2):giab008.
26. Lemey P, Rambaut A, Drummond AJ, Suchard MA. Bayesian Phylogeography Finds Its Roots. PLOS Comput Biol. 2009 Sep 25;5(9):e1000520.
27. Suchard MA, Lemey P, Baele G, Ayres DL, Drummond AJ, Rambaut A. Bayesian phylogenetic and phylodynamic data integration using BEAST 1.10. Virus Evol. 2018 Jan 1;4(1):vey016.
28. Gill MS, Lemey P, Faria NR, Rambaut A, Shapiro B, Suchard MA. Improving Bayesian Population Dynamics Inference: A Coalescent-Based Model for Multiple Loci. Mol Biol Evol. 2013 Mar 1;30(3):713–24.
29. Rambaut A, Drummond AJ, Xie D, Baele G, Suchard MA. Posterior Summarization in Bayesian Phylogenetics Using Tracer 1.7. Syst Biol. 2018 Sep 1;67(5):901–4.
30. Bedford T, Cobey S, Beerli P, Pascual M. Global Migration Dynamics Underlie Evolution and Persistence of Human Influenza A (H3N2). PLOS Pathog. 2010 May 27;6(5):e1000918.
31. Dudas G, Bedford T. The ability of single genes vs full genomes to resolve time and space in outbreak analysis. BMC Evol Biol. 2019 Dec;19(1):232.
32. Figgins MD, Bedford T. SARS-CoV-2 variant dynamics across US states show consistent differences in effective reproduction numbers [Internet]. medRxiv; 2022 [cited 2023 May 4]. p. 2021.12.09.21267544. Available from: https://www.medrxiv.org/content/10.1101/2021.12.09.21267544v2
33. Fauver JR, Petrone ME, Hodcroft EB, Shioda K, Ehrlich HY, Watts AG, et al. Coast-to-Coast Spread of SARS-CoV-2 during the Early Epidemic in the United States. Cell. 2020 May 28;181(5):990-996.e5.
34. Müller NF, Rasmussen D, Stadler T. MASCOT: parameter and state inference under the marginal structured coalescent approximation. Bioinformatics. 2018 Nov 15;34(22):3843–8.
35. Müller NF, Rasmussen DA, Stadler T. The Structured Coalescent and Its Approximations. Mol Biol Evol. 2017 Nov 1;34(11):2970–81.
36. Müller NF, Dudas G, Stadler T. Inferring time-dependent migration and coalescence patterns from genetic sequence and predictor data in structured populations. Virus Evol. 2019 Jul 1;5(2):vez030.
37. Bouckaert R, Vaughan TG, Barido-Sottani J, Duchêne S, Fourment M, Gavryushkina A, et al. BEAST 2.5: An advanced software platform for Bayesian evolutionary analysis. PLOS Comput Biol. 2019 Apr 8;15(4):e1006650.
38. Baele G, Lemey P, Rambaut A, Suchard MA. Adaptive MCMC in Bayesian phylogenetics: an application to analyzing partitioned data in BEAST. Bioinforma Oxf Engl. 2017 Jun 15;33(12):1798–805.

39. Müller NF, Bouckaert RR. Adaptive Metropolis-coupled MCMC for BEAST 2. PeerJ. 2020;8:e9473.
40. Huddleston J, Hadfield J, Sibley TR, Lee J, Fay K, Ilcisin M, et al. Augur: a bioinformatics toolkit for phylogenetic analyses of human pathogens. J Open Source Softw. 2021;6(57):2906.
41. Vaughan TG. IcyTree: rapid browser-based visualization for phylogenetic trees and networks. Valencia A, editor. Bioinformatics. 2017 Aug 1;33(15):2392–4.
42. VanderPlas J, Granger B, Heer J, Moritz D, Wongsuphasawat K, Satyanarayan A, et al. Altair: Interactive statistical visualizations for python. J Open Source Softw. 2018;3(32):1057.
43. Müller NF, Wagner C, Frazar CD, Roychoudhury P, Lee J, Moncla LH, et al. Viral genomes reveal patterns of the SARS-CoV-2 outbreak in Washington State. Sci Transl Med [Internet]. 2021 May 26 [cited 2021 Jun 3];13(595). Available from: https://stm.sciencemag.org/content/13/595/eabf0202
44. Paredes MI, Perofsky AC, Frisbie L, Moncla LH, Roychoudhury P, Xie H, et al. Local-Scale phylodynamics reveal differential community impact of SARS-CoV-2 in metropolitan US county [Internet]. medRxiv; 2022 [cited 2023 Apr 19]. p. 2022.12.15.22283536. Available from: https://www.medrxiv.org/content/10.1101/2022.12.15.22283536v1
45. Ma J. Estimating epidemic exponential growth rate and basic reproduction number. Infect Dis Model. 2020 Jan 8;5:129–41.
46. Wallinga J, Lipsitch M. How generation intervals shape the relationship between growth rates and reproductive numbers. Proc R Soc B Biol Sci. 2007 Feb 22;274(1609):599–604.
47. Tran-Kiem C, Bedford T. Estimating the reproduction number and transmission heterogeneity from the size distribution of clusters of identical pathogen sequences [Internet]. Epidemiology; 2023 Apr [cited 2023 Apr 19]. Available from: http://medrxiv.org/lookup/doi/10.1101/2023.04.05.23287263
48. Lloyd-Smith JO, Schreiber SJ, Kopp PE, Getz WM. Superspreading and the effect of individual variation on disease emergence. Nature. 2005 Nov;438(7066):355–9.
49. De Maio N, Wu CH, O'Reilly KM, Wilson D. New Routes to Phylogeography: A Bayesian Structured Coalescent Approximation. PLoS Genet. 2015 Aug 12;11(8):e1005421.
50. Layan M, Müller NF, Dellicour S, De Maio N, Bourhy H, Cauchemez S, et al. Impact and mitigation of sampling bias to determine viral spread: Evaluating discrete phylogeography through CTMC modeling and structured coalescent model approximations. Virus Evol. 2023 Jan 1;9(1):vead010.
51. Blumberg S, Lloyd-Smith JO. Inference of R0 and Transmission Heterogeneity from the Size Distribution of Stuttering Chains. PLOS Comput Biol. 2013 May 2;9(5):e1002993.
52. Riser AP. Epidemiologic and Clinical Features of Mpox-Associated Deaths — United States, May 10, 2022–March 7, 2023. MMWR Morb Mortal Wkly Rep [Internet]. 2023 [cited 2023 Apr 19];72. Available from: https://www.cdc.gov/mmwr/volumes/72/wr/mm7215a5.htm
53. Lemey P, Ruktanonchai N, Hong SL, Colizza V, Poletto C, Van den Broeck F, et al. Untangling introductions and persistence in COVID-19 resurgence in Europe. Nature. 2021 Jul;595(7869):713–7.
54. Whittles LK, White PJ, Didelot X. A dynamic power-law sexual network model of gonorrhoea outbreaks. PLOS Comput Biol. 2019 Mar 8;15(3):e1006748.
55. Fink DL, Callaby H, Luintel A, Beynon W, Bond H, Lim EY, et al. Clinical features and management of individuals admitted to hospital with monkeypox and associated

complications across the UK: a retrospective cohort study. Lancet Infect Dis. 2023 May 1;23(5):589–97.
56. Mitjà O, Alemany A, Marks M, Mora JIL, Rodríguez-Aldama JC, Silva MST, et al. Mpox in people with advanced HIV infection: a global case series. The Lancet. 2023 Mar 18;401(10380):939–49.
57. McCrone JT, Hill V, Bajaj S, Pena RE, Lambert BC, Inward R, et al. Context-specific emergence and growth of the SARS-CoV-2 Delta variant. Nature. 2022 Oct;610(7930):154–60.
58. Dye C, Kraemer MUG. Investigating the monkeypox outbreak. BMJ. 2022 May 26;377:o1314.
59. Mpox | Disease Directory | Travelers' Health | CDC [Internet]. [cited 2023 Apr 19]. Available from: https://wwwnc.cdc.gov/travel/diseases/mpox?CDC_AA_refVal=https%3A%2F%2Fwww.cdc.gov%2Fpoxvirus%2Fmpox%2Ftravel%2Findex.html
60. Frey SE, Wald A, Edupuganti S, Jackson LA, Stapleton JT, Sahly HE, et al. Comparison of lyophilized versus liquid modified vaccinia Ankara (MVA) formulations and subcutaneous versus intradermal routes of administration in healthy vaccinia-naïve subjects. Vaccine. 2015 Sep 22;33(39):5225–34.
61. Wolff Sagy Y, Zucker R, Hammerman A, Markovits H, Arieh NG, Abu Ahmad W, et al. Real-world effectiveness of a single dose of mpox vaccine in males. Nat Med. 2023 Mar;29(3):748–52.
62. Clay PA, Asher JM, Carnes N, Copen CE, Delaney KP, Payne DC, et al. Modelling the impact of vaccination and sexual behavior change on reported cases of mpox in Washington D.C [Internet]. medRxiv; 2023 [cited 2023 Apr 19]. p. 2023.02.10.23285772. Available from: https://www.medrxiv.org/content/10.1101/2023.02.10.23285772v1
63. Yang S, Guo X, Zhao Z, Abudunaibi B, Zhao Y, Rui J, et al. Possibility of mpox viral transmission and control from high-risk to the general population: a modeling study. BMC Infect Dis. 2023 Feb 24;23(1):119.
64. Brand SPC, Cavallaro M, Cumming F, Turner C, Florence I, Blomquist P, et al. The role of vaccination and public awareness in forecasts of Mpox incidence in the United Kingdom. Nat Commun. 2023 Jul 11;14(1):4100.
65. Bedford T, Greninger AL, Roychoudhury P, Starita LM, Famulare M, Huang ML, et al. Cryptic transmission of SARS-CoV-2 in Washington state. Science. 2020 Oct 30;370(6516):571–5.
66. Faria NR, Quick J, Claro IM, Thézé J, de Jesus JG, Giovanetti M, et al. Establishment and cryptic transmission of Zika virus in Brazil and the Americas. Nature. 2017 Jun;546(7658):406–10.

Supplementary Information

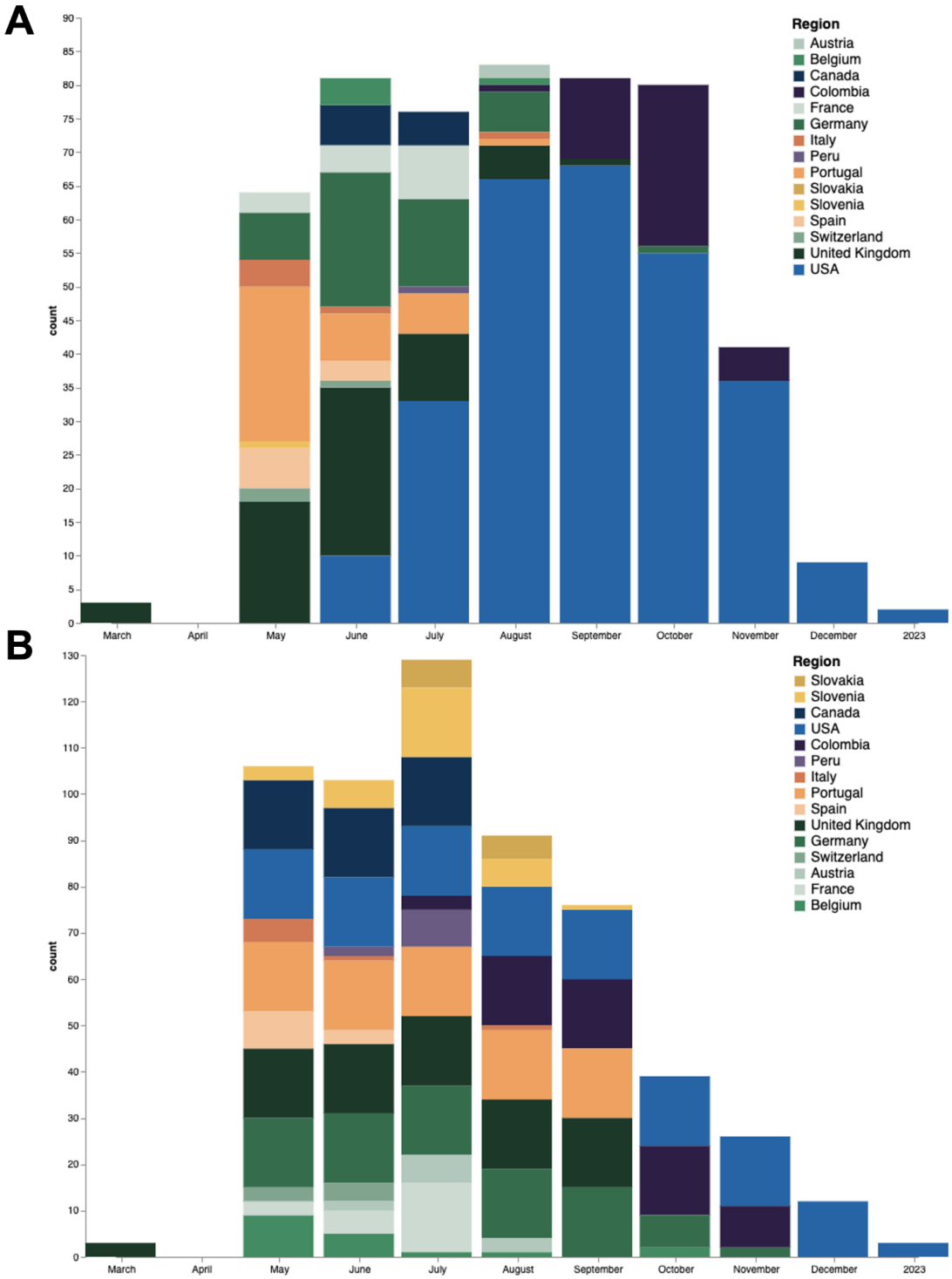

Supp. Fig. 1. Distribution of subsampled genomes. (A) Temporal Distribution of 1004 genomes used for phylogeographic analysis. Genomes were subsampled using confirmed case counts as weights. **(B)** Temporal distribution of 587 genomes used for MASCOT-GLM analysis. Subsampling was done to promote an equal number of samples from each deme for each month in order to upsample underrepresented countries.

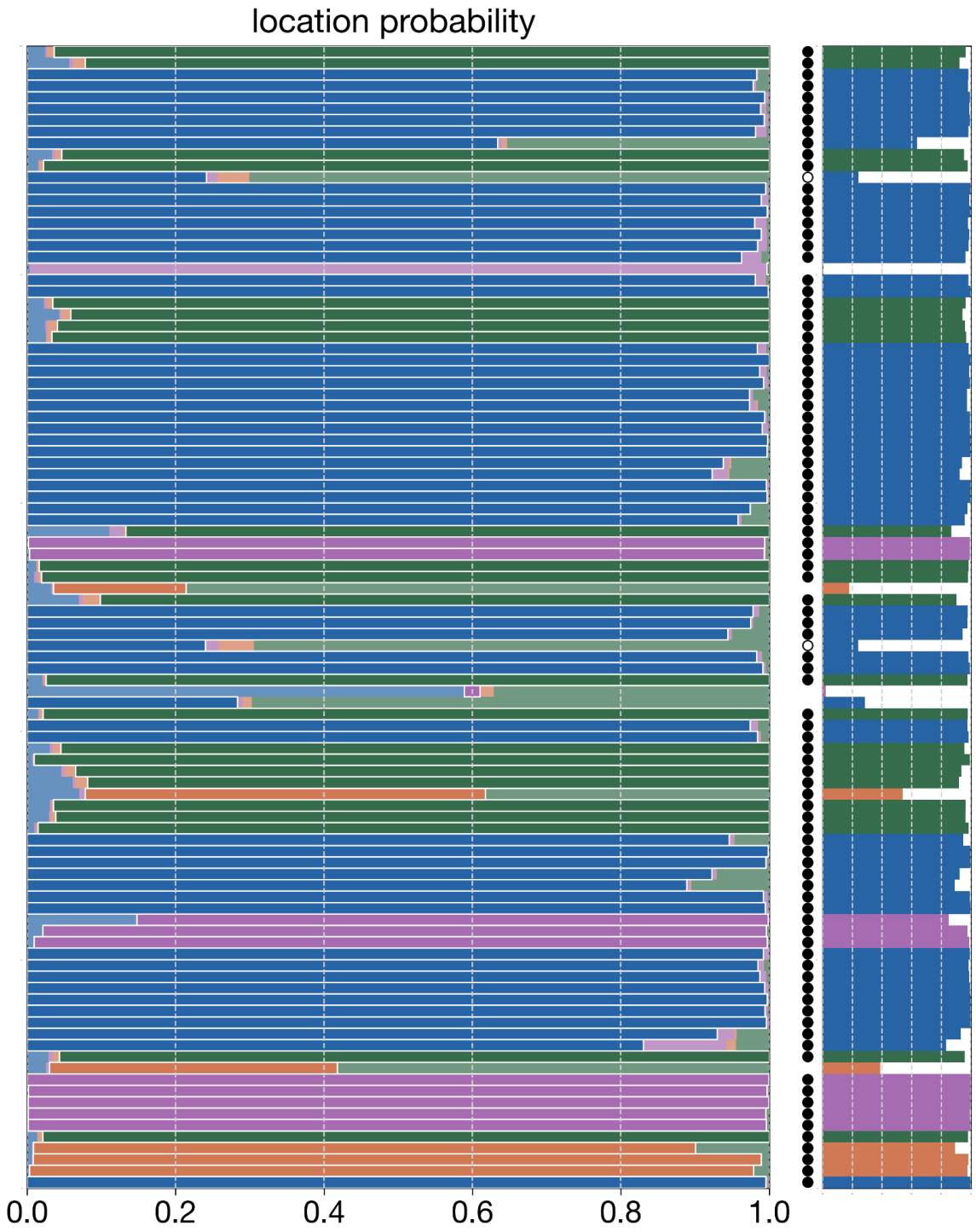

Supp. Fig. 2. Masked tip location inference. Horizontal bars indicate the posterior distribution of masked tip locations, coloured by region.. The correct location of each tip is outlined in white with the smaller plot to the right showing only the posterior probability of the correct location. Bars marked with an open circle indicate cases where the correct location is within the 95% credible set and solid circles indicate cases where the location with the most probability mass is also the correct location.

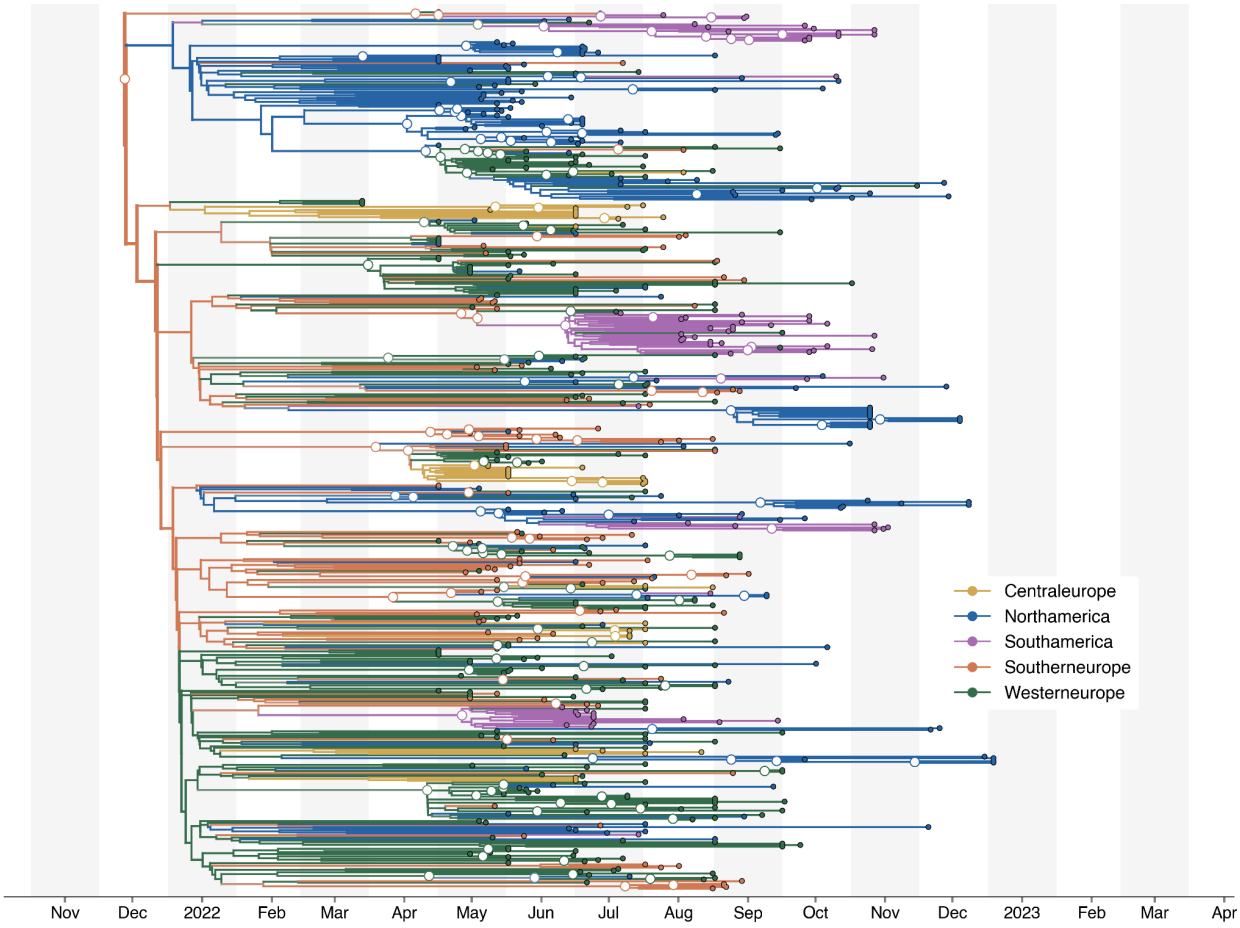

Supp. Fig. 3. The maximum clade credibility tree summary of the Bayesian inference conducted using MASCOT-GLM on 587 sequences. Colors correspond to the regions in the legend. Ancestral nodes with greater than 50% posterior support are highlighted with a white circle overlaid

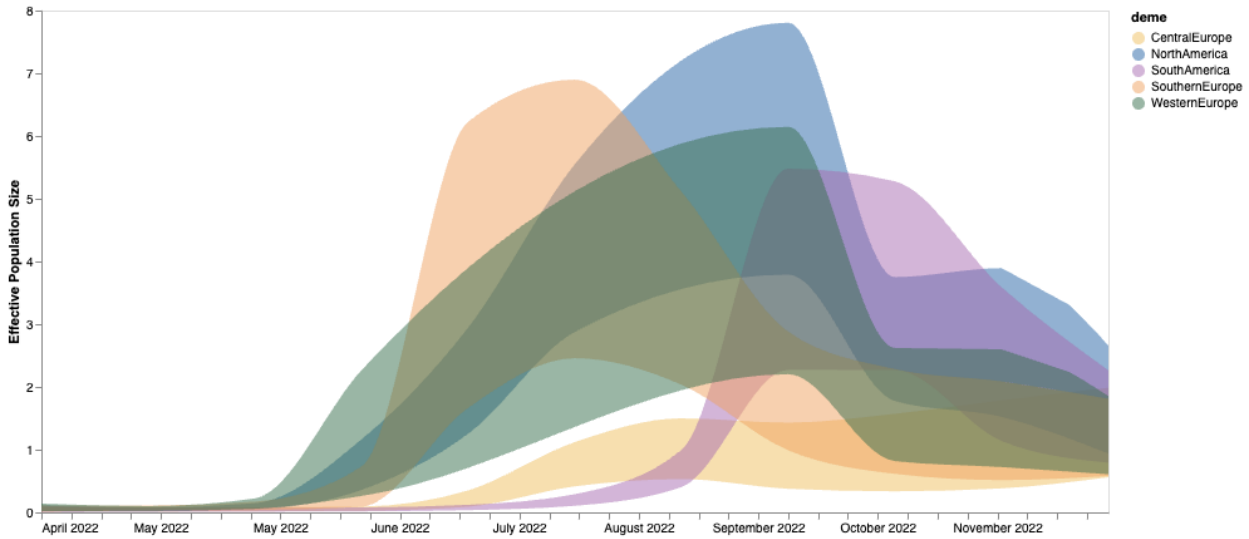

Supp. Fig. 4. Effective population size estimated via MASCOT-Skyline. Estimates of effective population sizes (NeTao in years) from April 2022 through December 2024 using 550 sequences subsampled equally throughout time. In contrast to the main MASCOT-GLM analysis, no empirical predictors were used, showing the extent of phylogenetic signal and uncertainty when using only genomes.

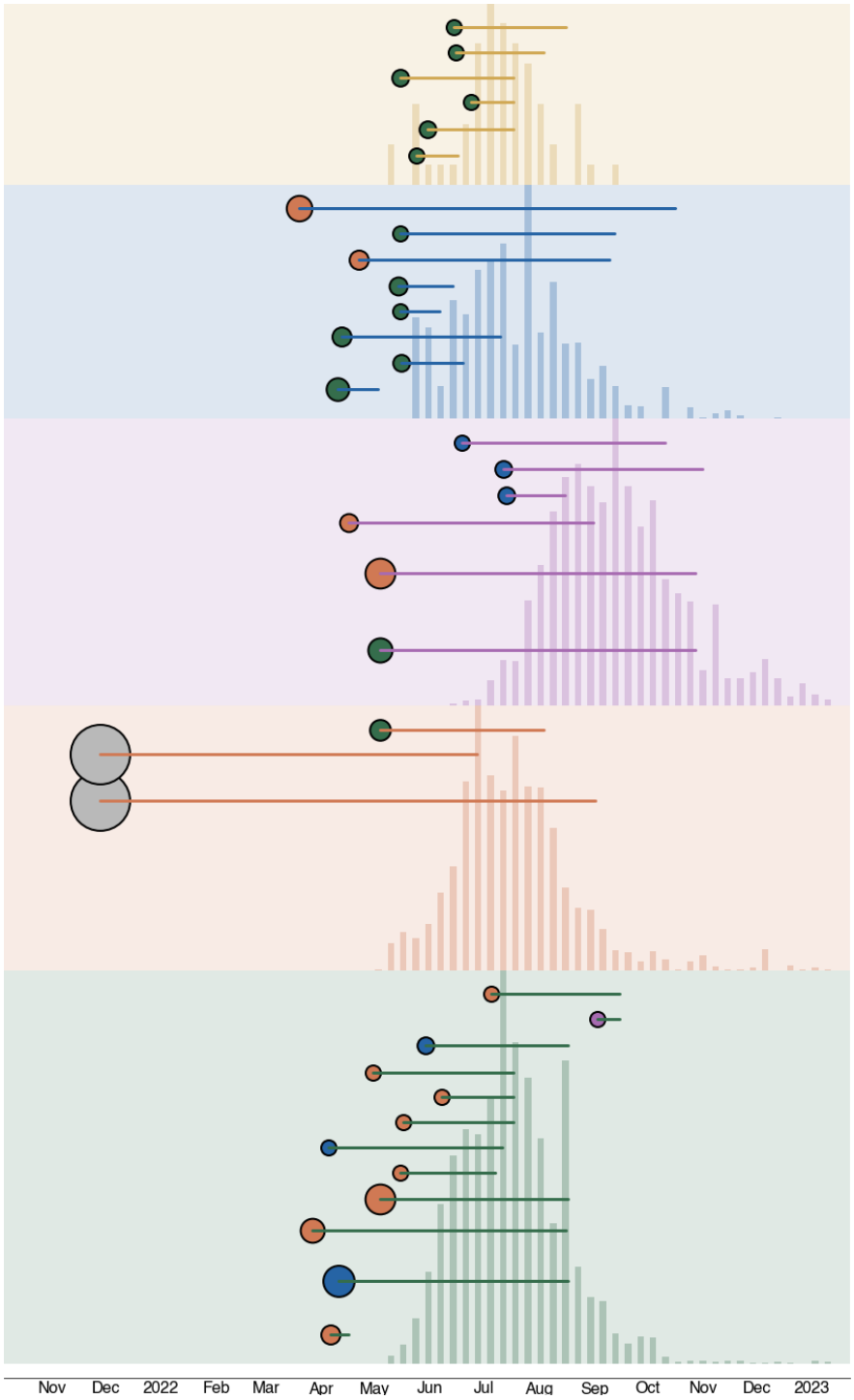

Supp. Fig. 5. Early underdetected introductions lead to longer transmission chains. Exploded subtrees for each region with only the introductions with greater than 50% posterior support. Color at introduction origin represents inferred source region and size of the circle at the origin is proportional to the number of downstream tips. Length of line coming out of each introduction origin represents the length of the transmission chain. Case counts are overlaid for each region

.

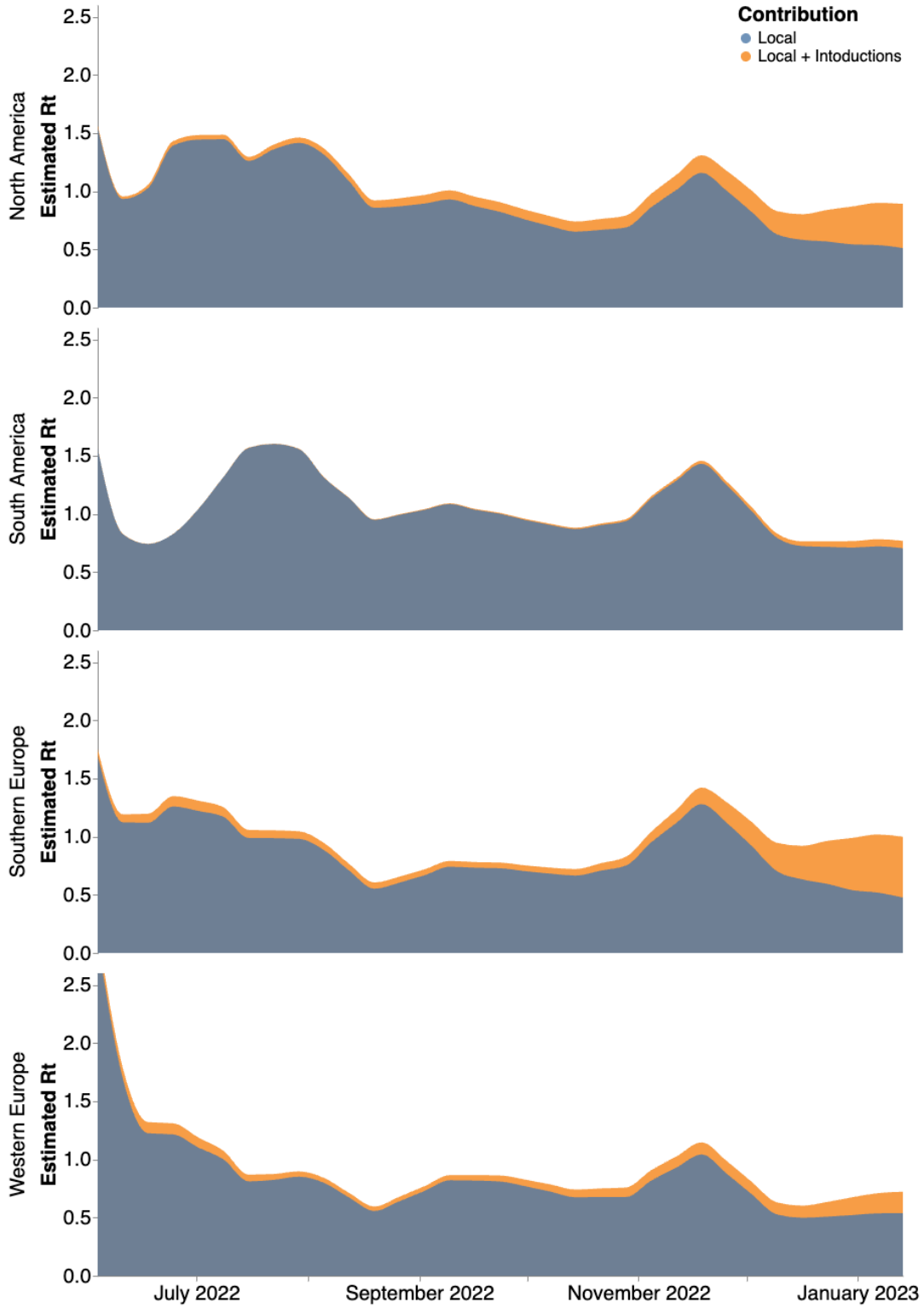

Supp. Fig. 6. Estimates of time-varying reproductive number (Rt) in four global regions. Estimates of Rt from April 2022 through December 2023 via MASCOT-GLM separated by source of contribution. Blue denotes local Rt without the influence of outside viral introductions while orange shows the added contribution of introductions. Central Europe was removed due to limited data on introductions

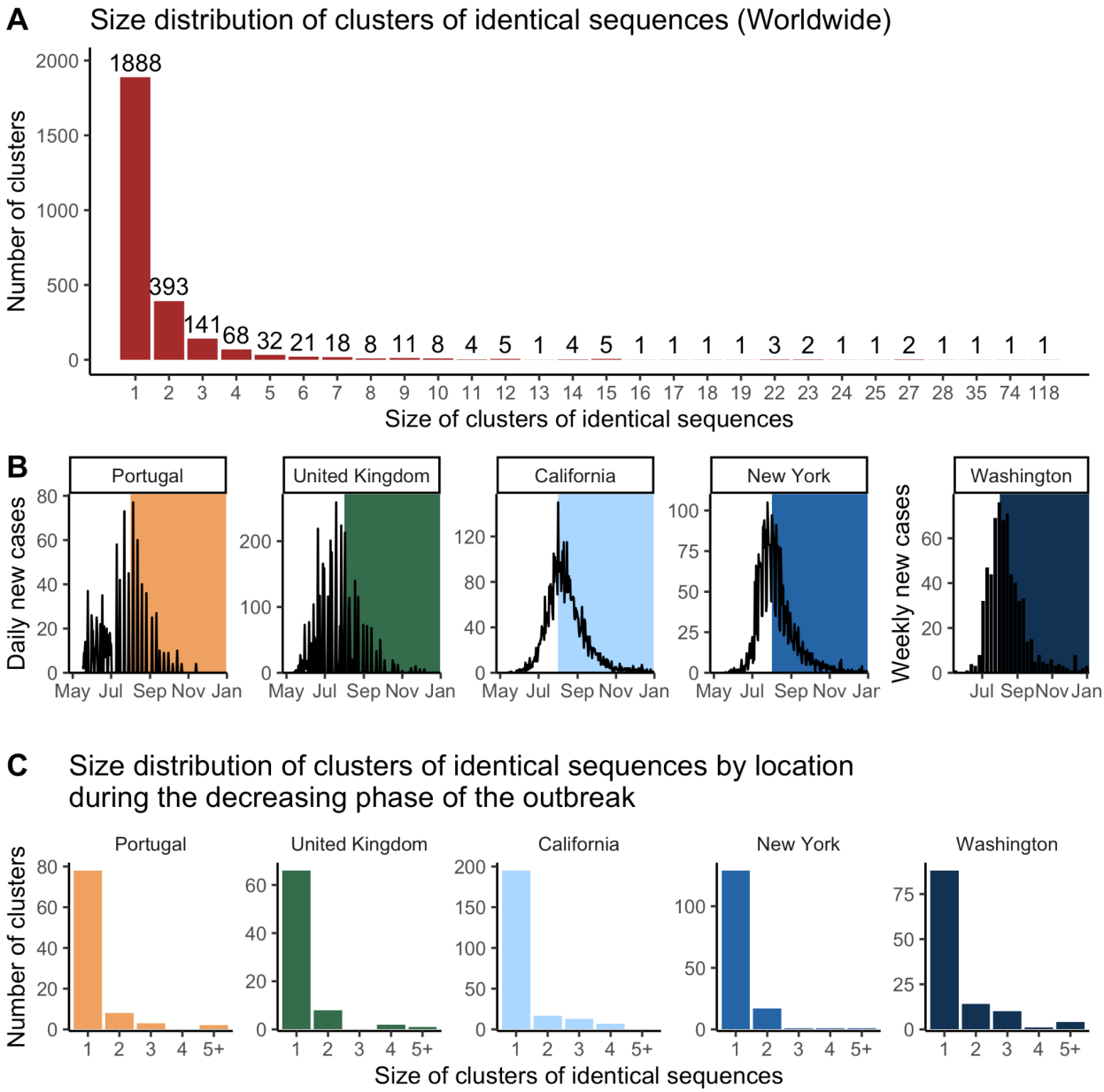

Supp. Fig. 7. Size distribution of clusters of identical mpox sequences. (A) Size distribution of clusters of identical mpox sequences worldwide. **(B)** Dynamics of mpox cases in the location of study. The coloured rectangles correspond to the study period. **(C)** Size distribution of clusters of identical mpox sequences by location during the decreasing phase of the outbreak (study period defined in B).

Supp. Table 1. Geocoding for various country and regional scales used in this study. DTA denotes the samples for the phylogeographic analysis which was subsampled using confirmed case counts as weights. MASCOT-GLM column denotes the sample for the phylodynamic inference which was subsampled by enforcing equal temporal sampling per country per month.

Region	Country	DTA	MASCOT-GLM
North America	Canada	27	45
	United States	533	120
Western Europe	Austria	3	11
	Germany	116	84
	Switzerland	7	7
	United Kingdom	94	78
	France	25	23
	Belgium	15	18
Central Europe	Slovakia	0	11
	Slovenia	0	31
Southern Europe	Italy	6	7
	Portugal	88	75
	Spain	9	11
South America	Colombia	77	57
	Peru	3	10

Supp. Table 2. Comparison of time to most recent common ancestor (TMRCA) by method. First two rows denote the comparison of TMRCA in the main datasets used which include three sequences from March 2022 which were found retrospectively in the UK. The last two rows represent the same analyses but without the three retrospective march 2022 samples.

Method	Mean	95% HPD	Tree Prior
With three retrospectively-collected March 2022 sequences from the UK			
DTA	2022-03-24	(2022-03-09 - 2022-03-27)	SkyGrid
MASCOT-GLM	2021-12-03	(2021-09-21 - 2022-02-01)	Approximate Structured Coalescent
Without March 2022 sequences from the UK			
DTA	2022-03-30	(2022-03-05 - 2022-04-19)	SkyGrid
MASCOT-GLM	2021-11-29	(2021-09-19 - 2022-01-28)	Approximate Structured Coalescent

Supp. Table 3. Reproduction numbers and dispersion parameter estimates from the analysis of the size distribution of clusters of identical sequences using a joint-likelihood. For each location, we report maximum likelihood estimates (MLE) along 95% likelihood profile confidence intervals. Different assumptions regarding the proportion of infections sequenced are explored. These estimates were obtained by allowing the reproduction numbers to vary between regions but assuming a similar value of the dispersion parameter *k* across locations.

Assumption regarding the proportion of infections detected	Location	*R* estimate (maximum likelihood estimate with 95% confidence interval)	*k* estimate (maximum likelihood estimate with 95% confidence interval)	Proportion of infected individuals with 0 offspring (obtained from *R* and *k* MLE)
10%	Portugal	0.87 (0.71-1.03)	0.16 (0.11-0.23)	74%
	United Kingdom	1.10 (0.98-1.22)		72%
	California (USA)	1.14 (1.08-1.20)		72%
	New York (USA)	1.05 (0.94-1.14)		72%
	Washington (USA)	1.06 (0.94-1.19)		72%
50%	Portugal	0.60 (0.44-0.80)	0.30 (0.18-0.54)	72%
	United Kingdom	0.89 (0.73-1.06)		66%
	California (USA)	0.94 (0.85-1.03)		65%
	New York (USA)	0.82 (0.69-0.94)		67%
	Washington (USA)	0.84 (0.69-1.02)		67%
100%	Portugal	0.46 (0.31-0.66)	0.36 (0.21-0.71)	74%
	United Kingdom	0.76 (0.59-0.95)		66%
	California (USA)	0.82 (0.72-0.92)		65%
	New York (USA)	0.68 (0.55-0.82)		68%
	Washington (USA)	0.70 (0.54-0.91)		68%

Supp. Table 4. Location-specific reproduction number and dispersion parameter estimates from the analysis of the size distribution of clusters of identical sequences. For each location, we report maximum likelihood estimates (MLE) along 95% likelihood profile confidence intervals. Different assumptions regarding the proportion of infections sequenced are explored.

Location	Assumption regarding the proportion of infections detected	*R* estimate (maximum likelihood estimate with 95% confidence interval)	*k* estimate (maximum likelihood estimate with 95% confidence interval)	Proportion of infected individuals with 0 offspring (obtained from *R* and *k* MLE)
Portugal	10%	0.8 (0.64-0.98)	0.09 (0.02-0.3)	81%
	50%	0.57 (0.40-0.79)	0.19 (0.04-1.8)	77%
	100%	0.45 (0.29-0.67)	0.23 (0.06-6.5)	78%
United Kingdom	10%	0.97 (0.81-1.12)	0.11 (0.03-0.34)	78%
	50%	0.76 (0.58-0.95)	0.23 (0.04-2.6)	72%
	100%	0.63 (0.45-0.84)	0.28 (0.05- >10)	72%
California (USA)	10%	1.03 (0.95-1.11)	0.07 (0.03-0.11)	83%
	50%	0.89 (0.8-0.98)	0.19 (0.08-0.42)	72%
	100%	0.79 (0.68-0.89)	0.25 (0.1-0.75)	70%
New York (USA)	10%	1.21 (1.14-1.28)	1.26 (0.37 - >10)	42%
	50%	0.92 (0.79-1.03)	1.04 (0.24- >10)	52%
	100%	0.75 (0.61-0.88)	0.99 (0.19- >10)	58%
Washington (USA)	10%	1.1 (0.99-1.21)	0.23 (0.07-0.72)	67%
	50%	0.85 (0.71-1.02)	0.38 (0.13-2.3)	64%
	100%	0.71 (0.55-0.9)	0.43 (0.16-2.8)	66%